Energy Spectra and Pitch Angle Distributions of Lightning-Induced Electron Precipitation: Analysis of an Event Observed on the S81-1(SEEP) Satellite

U. S. INAN

STAR Laboratory, Stanford University, Stanford, California

M. WALT, H. D. VOSS, AND W. L. IMHOF

Lockheed Palo Alto Research Laboratory, Palo Alto, California

Temporal and spectral signatures of a lightning-induced electron precipitation (LEP) burst observed on the S81-1 (SEEP) satellite are analyzed and compared with the predictions of a test particle model of the gyroresonant whistler-particle interaction in the magnetosphere. The flux to be detected by specific detectors on the low altitude ($\sim$ 220 km) satellite at $L \simeq 2.24$ is calculated in terms of the integral counting rate as a function of time and in terms of the dynamic energy spectra during the initial $\sim$ 300-ms precipitation pulse. For a whistler wave packet with frequency range 500 Hz to 6 kHz the dynamic energy spectra are found to depend sensitively on the electron angular distribution in the vicinity of the loss cone. In the case of a whistler wave originating in northern hemisphere lightning the maximum whistler-induced pitch angle scattering of electrons occurs near $\sim$ 10°S geomagnetic latitude. However, scattering occurring over the latitude range of $\sim$ 20°N to $\sim$ 20°S is found to be significant and contributes to the observed LEP pulse. The dynamic energy spectra of the LEP pulse and the temporal profile of the integral counting rate are consistent with the predictions of a test particle model of the gyroresonant scattering of the electrons by a whistler wave having an equatorial intensity at 6 kHz of $\sim$200 pT. The measured LEP pulse pitch angle distribution is wider than that estimated on the basis of the test particle model.

1. INTRODUCTION

The precipitation of energetic radiation belt electrons by lightning-generated whistler waves has attracted renewed attention in recent years. Early work on this topic included the first suggestions that lightning-induced precipitation may be important [*Dungey*, 1963; *Cornwall*, 1964], a rocket observation of a precipitating electron burst in correlation with a whistler [*Rycroft*, 1973], and the detection on the ground of subionospheric VLF signal perturbations in correlation with magnetospheric whistlers. The latter phenomenon, commonly referred to as the Trimpi effect, has been attributed to whistler-induced precipitation of > 40-keV electrons that perturb the ionospheric D region and therefore the subionospheric VLF signals [*Helliwell et al.*, 1973].

Recent observations of Trimpi effects, primarily at Palmer, Antarctica ($L \simeq 2.4$), have shown that lightning-induced precipitation commonly occurs at mid to low latitudes ($L < 3$) [*Carpenter and LaBelle*, 1982; *Leyser et al.*, 1984; *Inan et al.*, 1985a; *Inan and Carpenter*, 1987; *Carpenter and Inan*, 1987]. The first satellite based observation of a sequence of precipitating electron bursts in one-to-one association with lightning-generated whistlers was reported by *Voss et al* [1984]. A rocket-based observation of an electron precipitation burst in time correlation with atmospheric lightning has also been reported and the spectral structure of the lightning-induced electron precipitation (LEP) bursts has been discussed [*Goldberg et al.*, 1987].

Theoretical efforts have developed in parallel with these recent experimental findings, involving primarily the test particle modeling of the whistler-electron interaction in the magnetosphere [*Chang and Inan*, 1983, 1985a]. The capabilities of the theoretical model have reached a point where high-resolution dynamic spectra of whistler-induced precipitation pulses can be estimated [*Chang and Inan*, 1985b]. The model has also been applied to the comparison of precipitation induced by coherent and incoherent wave packets [*Inan*, 1987].

Comparison of theory and data is needed now in order to understand better the lightning-induced electron precipitation process and to identify those aspects of the interaction physics that determine such observable features as the temporal event signatures, the dynamic energy spectra, and the electron pitch angle distributions. Through such comparisons one can expect to identify the deficiencies of our present theoretical models. Accurate models are needed to assess the role of lightning-induced electron precipitation on the loss rates for the trapped radiation on a global scale.

The recent direct observations of LEP pulses in the course of the stimulated emission of energetic particles (SEEP) experiments conducted on the low-altitude S81-1 satellite provide a unique opportunity for detailed comparison of theory and data. This satellite was equipped with solid state detectors having high resolution in both time (64 ms) and energy (1.8 keV pulse height resolution over the range 6 to 1000 keV). In this study we use the test particle model to interpret the dynamic energy spectra, the temporal signature, and the pitch angle distribution of an individual whistler-induced electron precipitation pulse that was observed on September 9, 1982.
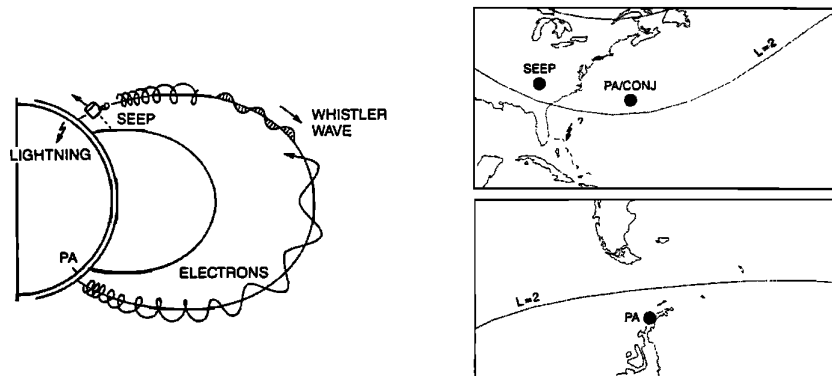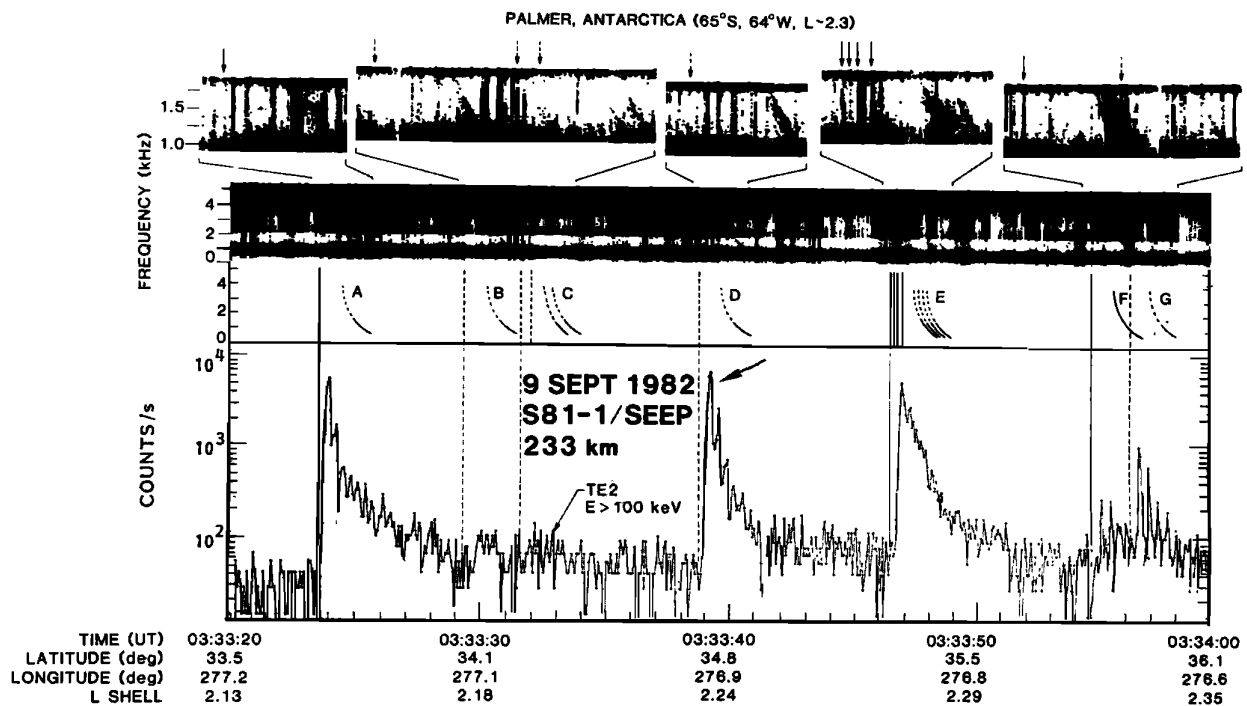
Fig. 1. The top panel shows the sequence of LEP bursts observed on the SEEP satellite in correlation with whistlers observed at Palmer, Antarctica [*Voss et al.*, 1984]. The pulse modeled in this paper is the first pulse in the LEP burst D, observed at $L \simeq 2.24$. The bottom left panel shows the interaction phenomenology, whereas the bottom right panel indicates the relative locations of Palmer Station, Antarctica, its magnetic conjugate point and the SEEP satellite at the time of the observations. The top panels show the VLF spectrograms and the scaled whistlers and spherics. The uppermost insets show the Palmer VLF data with an expanded time scale for the seven LEP events. The solid vertical lines represent spherics that were directly identified on these and other records, while the dashed lines represent time estimates based on the dispersion properties of the whistlers. The first pulse in LEP burst D is marked with an arrow and is the subject of the analysis presented in this paper.

2. REVIEW OF OBSERVATIONS

The LEP event sequence observed on the SEEP (S81-1) satellite on September 9, 1982, and the associated whistler spectra observed at Palmer station are shown in Figure 1. The particle data shown were obtained with an electron spectrometer designated TE2 with a ±20° field of view and aligned at an angle of near 90° with respect to the local magnetic field during the time of the observations. This detector had a geometric factor of 0.17 cm² sr and an energy resolution of 1.2 keV FWHM [*Voss et al.*, 1982a]. As noted in the original paper [*Voss et al.*, 1984], the events marked

A through G differ considerably in terms of the peak count rates for the bursts as well as the apparent whistler field strength. The LEP bursts associated with events B and C are relatively weak on the counting rate display of Figure 1 but are more prominent in the differential energy spectrum [*Voss et al.*, 1984]. We note that some of the larger events (A, D and E) are associated with the weaker whistlers observed at Palmer, whereas a weaker event such as event F is correlated with a stronger Palmer whistler. This circumstance can be ascribed to the longitude separation (~ 2000 km) between the satellite and the Palmer conjugate region so that strong electron events A, D, and E may have been

caused by lightning discharges close to the satellite but far away from the Palmer meridian. Weaker LEP events would result from lightning flashes at some distance from the satellite position.

Characteristics of the First LEP Pulse in Event D

For the following analysis we consider the LEP burst marked D that was observed at $L \simeq 2.24$. Event D was chosen for study since this burst is associated with a single whistler element and since the counting levels are high enough for the extraction of significant spectral and temporal information. The general features of the other LEP bursts are similar in terms of temporal signatures, although the peak intensity levels for integrated flux vary from ~ 170 to ~ 9500 counts/s. Variations in the widths of the individual pulses constituting the LEP bursts are also apparent from Figure 1.
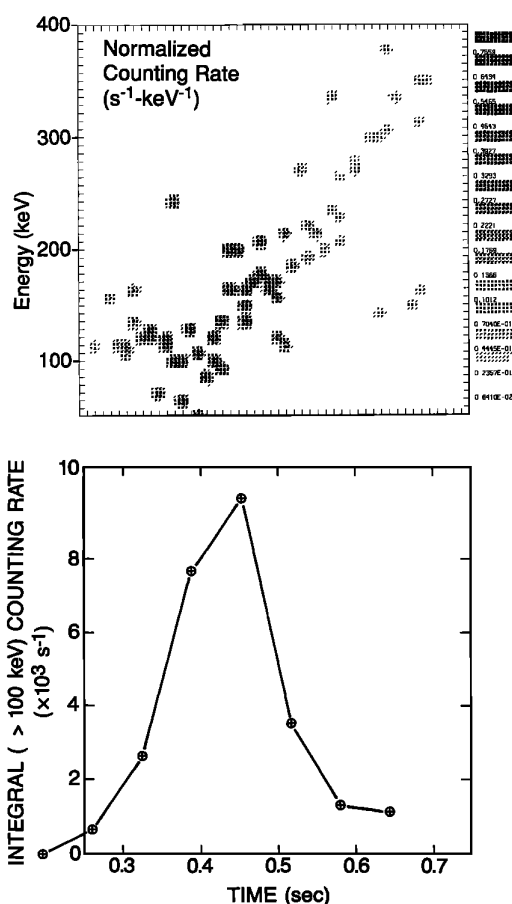

Fig. 2. The dynamic energy spectrum (top panel) and integral (> 100 keV) counting rate (bottom panel) for the first pulse of LEP burst D (Figure 1) as measured by the TE2 detector. For the integral counting rate the data points represent measurement samples taken at 64-ms intervals. The time reference $t = 0$ represents the occurrence time of the causative lightning discharge as estimated from the radio atmospheric observed at Palmer in conjunction with the whistler time correlated with LEP event D. The dynamic spectra (top panel), showing differential flux as a function of energy and time, is normalized so that the maximum value is unity. The 16 shade levels shown are equally spaced on a logarithmic scale.

For the purposes of this paper, we are interested in the very first pulse within the LEP event D, shown with an arrow in Figure 1. This pulse is interpreted to be a direct result of the cyclotron resonance interaction of trapped electrons with the whistler wave and should therefore exhibit temporal and spectral signatures that can be compared with the whistler-particle interaction theory. The successive multiple peaks that constitute this event (Figure 1) as well as others are interpreted as multiple bounces of the particle bunch between northern and southern hemispheres [*Voss et al.*, 1984]. Thus the temporal and spectral signatures of these subsequent pulses are significantly distorted due to their interactions with the atmosphere. An expanded plot of the time dependence of this first peak of event D is shown in Figure 2b.

For comparison with theory we use three different measures of the initial pulse in event D, namely, (1) the temporal variation of the integral count rate measured with the TE2 detector, shown in 2b (2) the dynamic energy spectra of the LEP pulse, i.e., the energy content of the LEP pulse as a function of time as given in Figure 2a, and (3) the pitch angle distribution as represented by counting ratios of detectors oriented at different directions with respect to the magnetic field. In Figure 2 the time $t = 0$ represents the deduced time of the lightning flash (to within ~ 30 ms) associated with the whistler of event D. The dynamic energy spectra are of particular importance, since this feature of a wave-induced precipitation event has been computed [*Chang and Inan*, 1985b], but previously its comparison with experimental data was not possible due to the lack of particle data with sufficiently high energy and time resolution.

On the S81-1 satellite the dynamic spectra were measured by means of a first-serve-sampling technique based on the pulse height analysis of the first pulse recorded in each 4-ms sampling interval [*Voss et al.*, 1982b]. While this technique perserves the original spectral form, it is statistically limited since for high counting rates only a fraction of counts are used to generate the spectrum. To compensate for this effect, the spectrum measured using the pulse height analysis technique was multiplied by a factor derived from the integral counter, which counts all pulses above the analyzer threshold for the duration of the spectrum accumulation. The resultant dynamic spectrum for the first pulse in event D is shown in the top panel of Figure 2. The most notable characteristic is the rise in average energy from about 100 keV to 300 keV during the pulse interval of ~ 300 ms.

The SEEP experiment on the low-altitude S81-1 satellite did not have the detectors needed for high-resolution pitch angle measurements. During the observation of the LEP event sequence shown in Figure 1 on September 9, 1982, three electron detectors on the S81-1 satellite registered counts. Two detectors had $\pm 20°$ field of view and their central axes were pointed at angles with respect to the magnetic field of 92° and 57°, and one detector with a field of view of $\pm 30°$ was pointed at an angle of 24°. These measurements are by themselves not sufficient to estimate the angular distribution of the LEP pulse without knowing the general shape of the distribution. However, a useful comparison between theory and measurement can be made by using the theoretically computed pitch angle distribution of the LEP pulse to estimate the counting rates that would be measured by the three detectors. This analysis is presented in section 4.

Whistler Wave Characteristics

The absence of in situ wave measurements makes the comparison with theory particularly difficult since the frequency spectrum and absolute intensity of the whistler waves associated with the observed LEP events are not known.

For some of the better-defined whistlers observed at Palmer on September 9, 1982, most of the wave energy was confined to the frequency range of 500 Hz to 6 kHz. The fact that the whistler associated with event D was detectable over a more limited range can be attributed to the fact that this relatively weak whistler is likely to have exited the magnetosphere at a siginificant distance from the Palmer Station. Thus the frequency range observed at Palmer would be affected by propagation in the Earth-ionosphere waveguide. In our modeling we have considered the whistler wave to have constant power spectral density over the frequency range of 500 Hz to 6 kHz.

The whistler wave intensity measured on the ground is not a reliable estimate of the field intensity in the magnetosphere because (1) the spreading losses in the magnetosphere depend upon whether the wave was ducted or non-ducted, (2) the D region absorption [Helliwell, 1965] and the earth-ionosphere waveguide attenuation are highly variable [Tsuruda et al.,1982; Crary, 1961], and (3) the ionospheric exit points for the whistlers and thus the distance to Palmer are not known. In this paper we initially adopt a value of $B_w = 100$ pT at 6 kHz as the whistler wave intensity at the equator to illustrate the single particle trajectories and the dependence of the LEP burst characteristics on the trapped particle distribution. This value of B_w is consistent with a crude estimate based on the intensity of the ducted whistler measured at Palmer (~ 15 μV/m at 1.2 kHz) and on the assumption that this whistler exited from the magnetosphere at the southern end of the SEEP field line (~ 2000 km due west of Palmer). The whistler field intensity is not critical to the determination of the energy spectra and temporal signatures of the LEP bursts but becomes an important factor when comparing the measured pitch angle distributions and absolute flux levels with theoretical estimates. In section 4, we compare results for B_w=100, 200, and 300 pT to illustrate the role of the whistler intensity in determining the characteristics of the LEP pulse.

We note that although the associated whistler for event D was relatively weak, the peak amplitude measured at Palmer was 15 dB above the noise background. Any other whistler components that may have been present (and that were not detectable) would have to be at least 15 dB lower in intensity and would therefore not significantly affect the determination of the timing of the LEP pulse.

Cold Plasma Density

The usual whistler dispersion analysis method [e.g., Carpenter and Smith, 1964] could not be applied directly to the September 9, 1982, whistlers, because of the limited frequency range over which they were defined on the records. However, their dispersion characteristics below 2 kHz were identical within measurement error of about 3% to those of well-defined whistlers measured at Palmer on March 30, 1983. The latter were observed at a similar local time and under similar magnetic and seasonal conditions, and the path L value of $L = 2.3 \pm 0.07$ and equatorial plasma density of $N_{eq} = 2000 \pm 300$ cm^{-3} were determined using whistler

analysis [Inan and Carpenter, 1987]. That the whistler path was indeed slightly equatorward of Palmer, at $L \simeq 2.4$, is consistent with the occurrence of whistler-associated particle precipitation effects (Trimpi events) on the approximately north-south path of NAA (17.8 kHz) from Cutler, Maine, to Palmer [Voss et al., 1984]. For the purposes of the modeling in this paper, we use $N_{eq} = 2000$ cm^{-3} as the equatorial cold plasma density at $L = 2.24$. In view of the uncertainties in other parameters used for our model calculation, the uncertainty in N_{eq} is not critical. The whistler propagation delay and the resonant particle velocity are, respectively, proportional to $\sqrt{N_{eq}}$ and $(N_{eq})^{-1/2}$; thus, the time delay estimates would change by about 15% between the two extremes of 1700 cm^{-3} and 2300 cm^{-3}.

3. WHISTLER-PARTICLE INTERACTION

In this section we discuss aspects of the whistler-particle gyroresonance interaction that are of key importance in the interpretation of the SEEP observations, in particular the dependence of the projected whistler-induced scattering angle (i.e., $\Delta\alpha_{eq}$) on the particle energy and on the resonance location along the field line. Although various characteristics of the interaction of whistlers and energetic electrons have recently been studied using a test particle model [Chang et al., 1983; Chang and Inan, 1985a, b], the above mentioned aspects have not been explicitly discussed. The illustration of these features requires a detailed description of the interaction physics. In the following section we undertake this task and also briefly review the test particle model used to simulate the interaction of a whistler wave with a full distribution of electrons.

Resonance Velocity $v_R(z)$

A convenient single parameter which can be used to describe the effectiveness of the whistler-particle interaction for a longitudinally propagating (k parallel to B_0) whistler wave and for a particle with parallel velocity $v_\parallel$ and pitch angle α is the resonance velocity, given by

$$v_R(z) = \frac{1}{k(z)}\left[\frac{\omega_H(z)}{\gamma} - \omega(z)\right] \qquad (1)$$

In equation (1) $\gamma = (1 - v^2/c^2)^{-1/2}$, $v = v_\parallel/\cos\alpha$ is the particle velocity, z is the distance along the field line, $(\omega_H(z)/\gamma)$ is the electron gyrofrequency, $\omega(z)$ is the angular wave frequency, and $k(z)$ is the whistler mode wave number, which for longitudinal propagation is given by $k \simeq (18\pi\sqrt{N_e}/c)\sqrt{\omega/(\omega_H - \omega)}$, where N_e is the electron density and c is the speed of light. At any instant of time $\omega(z)$ is a function of position since dispersion separates the frequencies of the whistler wave train. Resonance between the wave and the particle occurs when $v_\parallel \simeq v_R$. The effectiveness of the resonant interaction depends on the gradient of v_R with respect to z in the vicinity of the $v_\parallel \simeq v_R$ point, since this gradient affects the length of the time interval in which resonance occurs.

If the resonance velocity v_R goes through a minimum in the vicinity of the resonant crossing, i.e., if $[\partial v_R/\partial z]_{v_\parallel} \simeq v_R = 0]$, the interaction is termed to be a "second-order" resonance [Helliwell, 1970; Carlson et al., 1985]. Second-order resonances generally result in a more effective interaction (e.g., higher net pitch angle scattering) than "first order" resonances where $\partial v_R/\partial z$ does not change
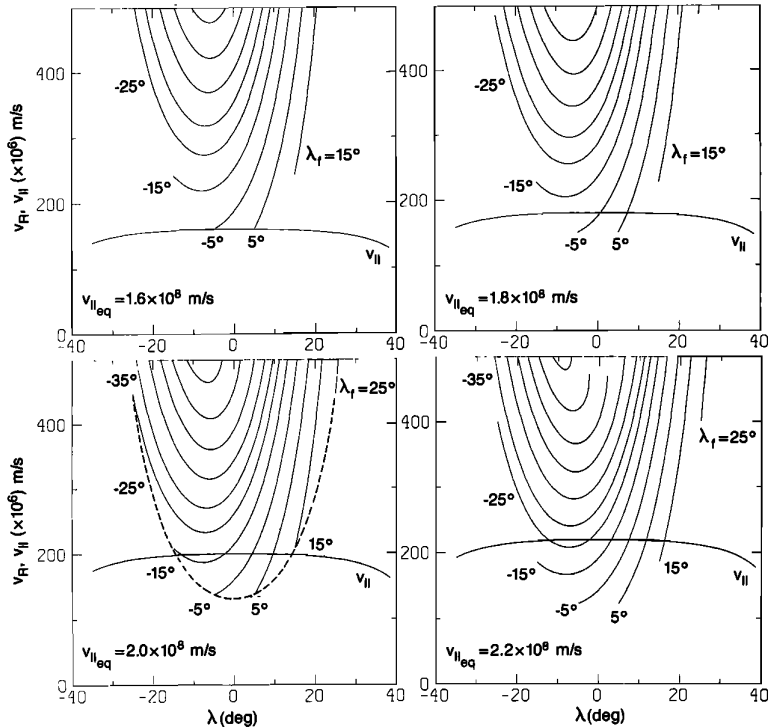
Fig. 3. Resonance velocity (v_R) curves for four values of $v_{\|eq}$. For each $v_{\|eq}$ the adiabatic variation of the particle parallel velocity $(v_\|)$ is shown as a nearly concave downward horizontal line. The v_R curve segments represent the resonance velocity which a particle with the given $v_{\|eq}$ must have to resonate with a whistler whose wavefront it encounters at different geomagnetic latitudes λ_f. The v_R were calculated directly from (1) using $\omega_H(z)$ and $N_e(z)$ obtained respectively from a centered dipole model of the magnetic field and a diffusive equilibrium model of the cold plasma density. The whistler wave was assumed to extend over the frequency range of 500 Hz to 6 kHz and to be propagating at $L = 2.24$ where the equatorial cold plasma density was taken to be $N_{eq} = 2000$ el/cc.

sign in the vicinity of the resonant $(v_\| \simeq v_R)$ encounter [Chang et al., 1983].

For monochromatic waves the resonance velocity variation $v_R(z)$ for particles encountering the wave packet at different points along the field line lies on a single curve [Chang et al., 1983]. In such a case the maximum interaction occurs at the geomagnetic equator, which is the point at which $v_R(z)$ is a minimum $(\partial v_R/\partial z = 0)$ [Inan et al., 1982]. For variable frequency waves such as the whistler, two important new factors must be considered. First, particles with different energies encountering the wave packet at the same point along the field line experience different v_R variations. Second, the whistler wave packet disperses as it propagates along the field line; as a result, the wave frequency variation $(d\omega/dz)$ experienced by particles of all energies becomes smaller with time (assuming that whistler frequencies are confined to a range below the nose frequency) [Helliwell, 1965]. The time variation of the whistler frequency ω can compensate for the latitude variation of the electron gyrofrequency ω_H and the wave number k, resulting in "second-order" resonance regions $(\partial v_R/\partial z = 0)$ well beyond the magnetic equator and the occurrence there of enhanced particle scattering. Note that the adiabatic variation of $v_\|$ with latitude is much smaller over the interaction regions of interest, especially for the particles in the vicinity of the loss cone.

To illustrate these effects we consider the interaction between the assumed whistler wave packet and electrons

having four different equatorial parallel velocities, namely, $v_{\|eq} = 1.6 \times 10^8, 1.8 \times 10^8, 2.0 \times 10^8$, and 2.2×10^8 m/s, or parallel energies of 93, 128, 175, and 241 keV. The particles of interest here have pitch angles within a few degrees of the loss cone ($\sim 14°$ at $L = 2.24$) so that the corresponding total energies are respectively, 99, 136, 186, and 245 keV. Particles in the $\sim 100 - 400$ keV range constituted most of the energy of the LEP bursts observed on September 9, 1982, and the behavior of those particles having energies > 250 keV is qualitatively similar as discussed below.

Figure 3 shows the resonance velocity curves for particles having the four different equatorial parallel velocities given above. For each $v_{\|eq}$, the adiabatic variation of the parallel velocity $v_\|$ is shown as a nearly horizontal curve together with the $v_R(z)$ curve segments for different latitudes λ_f at which the given particle encounters the leading edge of the whistler wave packet. The v_R was computed directly from (1) with $\omega_H(z)$ and $N_e(z)$ obtained respectively from a centered dipole model of the Earth's magnetic field and a diffusive equilibrium model of the cold plasma density along the field line [Angerami and Thomas, 1964]. The whistler is assumed to be propagating at $L = 2.24$ with the equatorial cold plasma density $N_{eq} = 2000$ cm^{-3}. The whistler is assumed to originate in northern hemisphere lightning so that the wave packet propagates from north ($\lambda > 0$) to south ($\lambda < 0$), while the particles travel in the opposite direction. As the whistler propagates along the field line, it continually meets particles with the selected value of $v_{\|eq}$, and

the corresponding $v_R(z)$ as determined by (1) varies as a function of λ_f. Since the whistler frequency decreases with time, it is expected that the second-order resonance point $(\partial v_R/\partial z=0)$ will occur at $\lambda_f < 0$ [*Helliwell*, 1970], as is the case in Figure 3.

Sample Electron Trajectories

The net scattering suffered by particles with a given $v_{\parallel eq}$ and encountering the whistler wave packet at a given point along the field line can be computed by integrating the complete equations of motion [*Inan et al.*, 1982] over the range of latitudes for which the electrons are nearly resonant with the wave, i.e., $v_{\parallel}(z) \simeq v_R(z)$. In doing so, we take full account of the wave-induced changes in both energy and pitch angle, although for parameters of interest here, the scattering in energy is much less important [*Roberts*, 1968; *Inan*, 1977]. For typical parameters of interest, accurate determination of the net pitch angle scattering requires that such an integration include contributions from regions where $v_{\parallel} \simeq v_R \pm 0.05 v_R$ [*Inan at al.*, 1978]. In our modeling calculations most of the particle trajectories are computed over the full range of latitudes (see, for example, the trajectories of Figures 6 and 7), except in those cases when the particle encounters the wave front at a latitude where $v_{\parallel}$ is within $\pm5\%$ of v_R so that the interaction starts with the particle initially being nearly resonant (see Figure 4 and middle panel of Figure 5). For the trajectories presented below, the spectral intensity of the whistler wave was assumed to be uniform over the frequency range of 500 Hz to 6 kHz with the equatorial wave magnetic field intensity at 6 kHz being 100 pT. The formats of Figure 4 and several following figures are identical. The top panel shows the variation of the local particle parallel velocity $v_{\parallel}$ together with v_R on an expanded scale, and the lower panel shows the equatorial pitch angle change $\Delta\alpha_{eq}$. The abscissa is geomagnetic latitude; the wave propagates from north to south (i.e., from positive to negative latitudes) and the par-
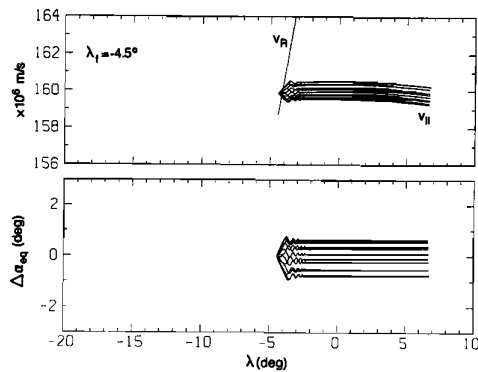

Fig. 4. Trajectories of 12 test particles uniformly distributed in initial Larmor phase and having an equatorial parallel velocity of $v_{\parallel eq} = 1.6 \times 10^8$ m/s and equatorial pitch angle of $\alpha_{eq} = 14.2^\circ$ (edge of loss cone at $L = 2.24$). The top panel shows the parallel velocities of the electrons entering the wave packet at $\lambda_f = -4^\circ$. The bottom panel shows the equatorial pitch angle change $\Delta\alpha_{eq}$ for each of the 12 test particles. The whistler wave intensity at 6 kHz near the equator was taken to be 100 pT with the intensity at other frequencies and/or at other locations along the field line being determined by signal dispersion, local refractive index, and conservation of signal energy within a duct.
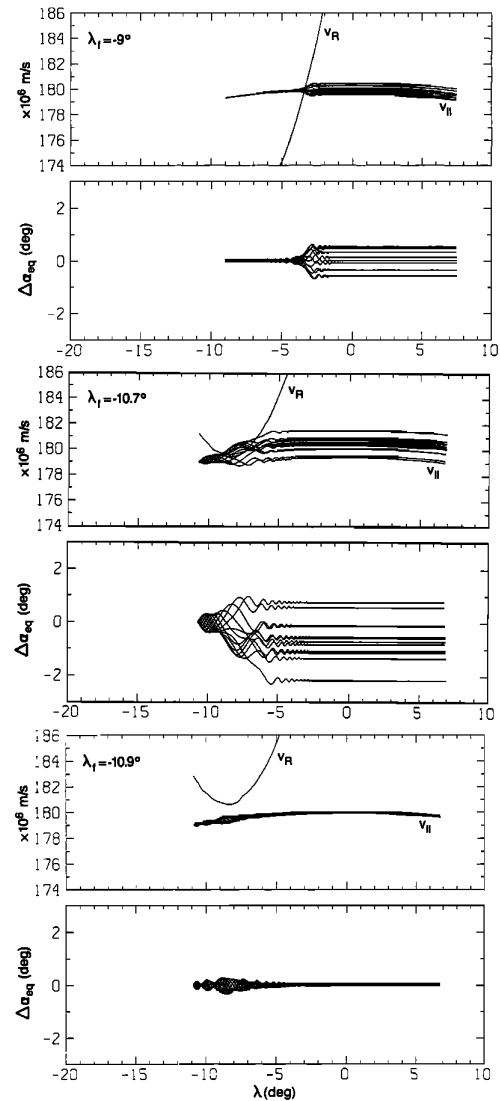

Fig. 5. Trajectories of 12 test particles uniformly distributed in initial Larmor phase and having an equatorial parallel velocity of $v_{\parallel eq} = 1.8 \times 10^8$ m/s and an equatorial pitch angle of $\alpha_{eq} = 14.2^\circ$. The top panels show results for $\lambda_f = -9^\circ$, the center panels are for $\lambda_f = -10.7^\circ$, whereas the bottom panels are for $\lambda_f = -10.9^\circ$. The format of this Figure is similar to that of figure 4.

ticles travel in the opposite direction. The trajectories of 12 particles uniformly distributed in initial Larmor phase are shown.

Interpreting the results given in Figure 3 for different values of $v_{\parallel eq}$, we see that for $v_{\parallel eq} = 1.6 \times 10^8$ m/s, only first-order resonance (crossing of the $v_{\parallel}$ and v_R curves) is possible and occurs for wave front positions of $-5^\circ < \lambda_f < 5^\circ$. However, significant scattering occurs in such first order resonance encounters, as illustrated in Figure 4 for the case of $\lambda_f = -4.5^\circ$. The net scattering experienced by the 12 test particles lies in the range $\pm1^\circ$.

For $v_{\parallel eq} = 1.8 \times 10^8$ m/s, we see from Figure 3 that first-order resonance encounters occur for wave front latitudes in the approximate range of $-10^\circ < \lambda_f < 10^\circ$. Second-order
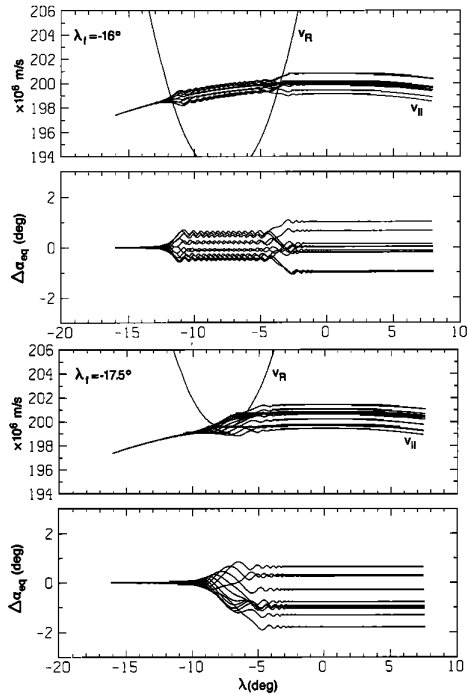
Fig. 6. Trajectories of 12 test particles uniformly distributed in initial Larmor phase and having an equatorial parallel velocity of $v_{\parallel eq} = 2.0 \times 10^8$ m/s and an equatorial pitch angle of $\alpha_{eq} = 14.2°$. The format of this figure is similar to those of Figures 4 and 5.

resonance is also possible for some latitude near $-10°$. The optimum condition for second-order resonance for particles with this $v_{\parallel eq}$ in fact occurs for $\lambda_f = -19.7°$; test particle trajectories for this case are given in the middle panel of Figure 5. The net scattering experienced by the particles shown lies in the range $-2.2° < \Delta\alpha_{eq} < 0.8°$. The top and bottom panels of Figure 5 show the results for respectively $\lambda_f = -9°$ and $-10.9°$; for $\lambda_f = -9°$ the interaction involves a first-order resonance resulting in net particle scatterings in the range $\pm 0.6°$. As shown in the lower panel of Figure 5, particles with this $v_{\parallel eq}$ encountering the wave front at latitudes λ_f slightly south of $-10.7°$ are only negligibly scattered since $v_{\parallel}$ does not cross $v_R(z)$.

For $v_{\parallel eq} = 2.0 \times 10^8$ m/s, first-order resonance occurs for an even larger range of λ_f, namely, $-15° < \lambda_f < 15°$. Multiple first-order encounters can occur for $\lambda_f = -15°$, and second-order resonance is clearly possible for λ_f slightly beyond $-15°$. This resonance occurs for $\lambda_f = -17.5°$, as illustrated by the particle trajectories in the bottom panels of Figure 6. For this case, the particle scatterings lie in the range $-1.8° < \Delta\alpha_{eq} < 0.7°$. The top panels of this figure show the multiple encounter case that occurs for $\lambda_f = -16°$. The first encounter results in scatterings of $\pm 0.6°$, and the second encounter increases the overall net scatterings of $\pm 1°$.

The behavior for $v_{\parallel eq} = 2.2 \times 10^8$ m/s is qualitatively similar to the previous case, except that first-order resonance occurs over a broader range of latitudes $(-25° < \lambda < 15°)$ and second-order resonance is possible for particles encountering the wave front at higher latitudes, specifically for

$\lambda_f \simeq -28.3°$. The test particle trajectories for this case are given in Figure 7. Note that the scattering range is less than that for Figure 6, being $-1.3° < \Delta\alpha_{eq} < 0.6°$.

While second-order resonance occurs for increasingly higher values of λ_f for increasing $v_{\parallel eq}$, its location is roughly the same for all three of the cases in Figures 5, 6, and 7 being at $\sim 7°$S geomagnetic latitude. This result is expected, since the locations of the minima in $v_R(z)$ are largely determined by the whistler dispersion $(\partial\omega/\partial z)$. In fact, as the whistler propagates and its wave front reaches higher southern latitudes, the minimum in $v_R(z)$ slowly moves toward the equator, since the frequency-time slope of the whistler is smaller near its tail [Chang et al., 1983].

The resonance velocity curves for two more values of $v_{\parallel eq}$, namely 2.6×10^8 and 2.8×10^8 m/s (i.e., 513 and 912 keV), are shown in Figure 8. Particles at these higher energies resonate with generally lower frequencies in the whistler wave packet; as a result the resonance points are closer to the tail of the whistler wave packet. For $v_{\parallel eq} = 2.6 \times 10^8$ m/s, second-order resonance occurs after the wave front has traversed the magnetosphere and arrived at the southern ionosphere. However, as was observed for the previous $v_{\parallel eq}$, the net scattering decreases with increasing parallel velocity. Note that the higher-energy particles go through their resonance regions faster, thus allowing less time for cumulative scattering. However, this effect is compensated by the fact that the wave force causing the scattering, i.e., $v_{\parallel} \times B_w$, is proportionally higher. The reduced net scattering at higher $v_{\parallel eq}$ results from the fact that for the same $\Delta v_{\parallel}$ the pitch angle scattering $\Delta\alpha$ is approximately proportional to $(v_{\parallel})^{-1}$ [Inan, 1987].

The salient features of the whistler-particle interaction as illustrated in Figures 3–8 can be summarized as follows:

1. Among particles that encounter the whistler wave front at a given location along the field line, those with energies below a certain value do not resonate with the wave and do not undergo significant scattering. For example, in Figure 3 for $\lambda_f = -15°$, particles with $v_{\parallel eq} = 1.6 \times 10^8$ m/s and $v_{\parallel eq} = 1.8 \times 10^8$ m/s are in this category. Particles with $v_{\parallel eq}$ such that the $v_{\parallel}$ curve becomes tangent to the v_R curve experience maximum scattering due to second-order
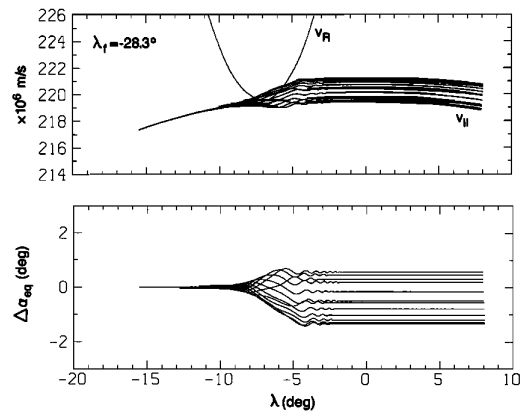

Fig. 7. Trajectories of 12 test particles uniformly distributed in initial Larmor phase and having an equatorial parallel velocity of $v_{\parallel eq} = 2.2 \times 10^8$ m/s and an equatorial pitch angle of $\alpha_{eq} = 14.2°$. The format of this figure is similar to those of Figures 4 and 5.
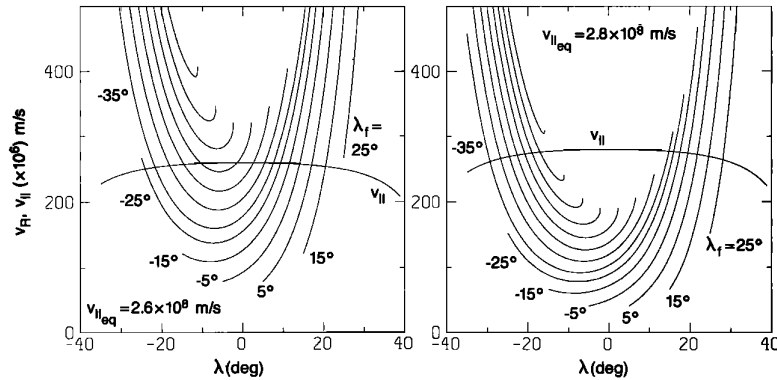
Fig. 8. Resonance velocity curves for $v_{\|eq} = 2.6 \times 10^8$ and 2.8×10^8 m/s. The format of this figure is identical to that of Figure 3.

resonance, whereas those with even higher energies generally experience two successive first-order resonances. The net scattering due to these first-order resonances is somewhat smaller than for second-order encounters, but such scattering is by no means negligible. At increasingly higher particle energies the net scattering slowly decreases with increasing energy.

2. In terms of pitch angle scattering as a function of location along the field line, electrons of a given energy interacting with the whistler before the wave front crosses the vicinity of the equator generally experience smaller net pitch angle changes $\Delta\alpha_{eq}$ than those encountering the wave front south of the equator. (Note that such encounters occurring before the equator are generally first-order resonances with scattering similar to that illustrated in Figure 4. Although trajectories of electrons encountering the wave prior to the equator are not explicitly shown here, examination of many such electron trajectories indicates that the net total scattering is small.) The largest individual particle scatterings $\Delta\alpha_{eq}$ are experienced by particles that undergo second-order resonance with the wave after it crosses the equator. For example, particles with equatorial parallel velocity of $v_\| = 2 \times 10^8$ m/s experience maximum interaction at $\sim 10°$ south of the geomagnetic equator. Although the pitch angle changes resulting from first-order resonance are somewhat smaller, they are not negligible. For a 100-pT whistler wave intensity, net pitch angle scattering of $0.5°-1°$ regularly results from first order resonance encounters that occur over a wide range of latitudes.

3. The whistler-particle gyroresonance interaction occurs over a wide range of latitudes and for a large range of particle energies. The scattering due to resonant encounters with particles of different energies occurring at different locations can be of comparable magnitude. Although second-order resonances tend to produce the largest scatterings, their contribution to the overall flux is limited by the fact that such resonances occur for a small range of particle velocities. First-order resonances occur for a much larger set of particles; the resulting individual particle scatterings are generally smaller, but the pitch angle changes are not smaller by more than a factor of ~ 2. Hence estimation of the overall flux signatures resulting from whistler-induced precipitation requires consideration of the convolved effects of interactions occurring over a range of latitudes and par-

ticle energies. Also important is the pitch angle and energy dependence of the particle distribution.

Test Particle Modeling of the Whistler Interaction With a Full Distribution of Electrons

The test particle model used in this paper has been discussed in detail in previous work [Inan et al., 1982; Chang et al., 1983; Chang and Inan, 1985b]. Here we provide a brief description of the essential features of the model that are relevant to the September 9, 1982, observations.

The whistler-particle interaction model simulates the interaction of the whistler wave and the particle distribution by computing the trajectories of a large number of test particles distributed in velocity space. The propagation of the whistler signal from one hemisphere to the other in a ducted mode (k parallel to $\mathbf{B_0}$) is assumed, and the interaction of the wave with particles of different energies as it propagates along the field line is taken into account. In the course of the propagation of the whistler wave packet from its hemisphere of origin (north) to the conjugate region (south) the leading edge of the wave pulse continually encounters new distributions of particles. Complete trajectories of individual test particles are computed to simulate the interaction with the wave of each such distribution of particles. Taking into account the wave and particle travel times, the precipitation flux resulting from the successive encounters with the wave of different distributions of particles are superposed to obtain the precipitated flux as a function of time and energy as would be observed at the hemisphere of origin (north) of the wave. In modeling the SEEP observations, the differential geometric factor across the viewing angle and the look direction of the TE2 detector at the time of the observations is considered, so that the counting rate that would be measured by this detector is directly computed [Chang and Inan, 1985b].

Note that the whistler waves that have scattered the electrons observed on September 9, 1982, may have been propagating in the nonducted mode, with k at an angle to $\mathbf{B_0}$. However, for a relatively smooth distribution of the background cold plasma and for wave frequencies of < 6 kHz at $L = 2.24$, the whistler ray paths are nearly field aligned even though the wave vector is not parallel to $\mathbf{B_0}$ [Edgar, 1986]. In such a circumstance the kinematics of the whistler wave
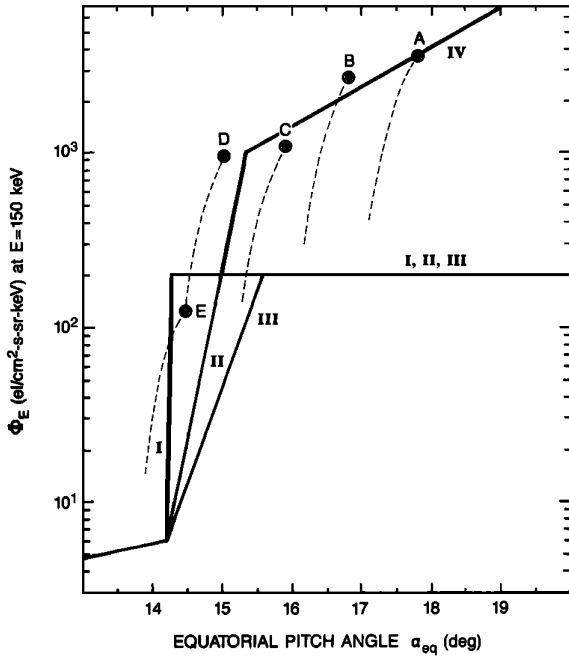
Fig. 9. The near loss cone distributions for 150-keV particles that are used for model calculations. The experimental values of the trapped electron flux inferred from SEEP measurements are shown as solid points. The pitch angle distributions were assumed to have the same shape (dashed lines) as those measured on the P78-1 satellite and were scaled in amplitude to give counting rates in agreement with those observed in five different southern hemisphere passes (labeled A through E) tabulated in Table A1. The best estimate for the trapped flux is represented by the heavy points, corresponding to electrons locally mirroring at 230 km altitude (see appendix for details).

and electron travel times and the resulting temporal variation and the dynamic energy spectrum of the LEP pulse are expected to be similar to that of ducted waves [*Inan et al.*, 1985*b*] even though the absolute flux levels and pitch angle distributions may be different.

4. COMPARISON OF MODEL RESULTS WITH EXPERIMENTAL DATA

In this section we present the results of the application of the test particle formulation to the parameters of the LEP event D illustrated in Figure 2. This event was observed at $L \simeq 2.24$, and the equatorial electron density as derived from whistler analysis was $N_{eq} \simeq 2000$ cm^{-3}. For the whistler wave we use a wave packet having constant power spectral density in the frequency range 500 Hz to 6 kHz, with the wave magnetic field at the equator at 6 kHz being 100, 200, or 300 pT as specified. The differential energy spectrum for the trapped energetic particle distribution immediately prior to the LEP event is taken to be

$$\Phi(\alpha_{eq}, E) \simeq g(\alpha_{eq})e^{-E/E_0} \qquad \alpha_{eq} \geq 14.15°$$

where $g(\alpha_{eq})$ is the pitch angle distribution. At the time of the S81-1 observations of LEP event D on September 9, 1982, the equatorial pitch angle corresponding to a local pitch angle of 90° at the satellite location was $\alpha_{eq} \simeq 14.15°$. Consequently, it was not possible to observe the trapped

electron distribution for $\alpha_{eq} \geq 14.15°$. However, data from S81-1 acquired during other times and orbits (primarily in the southern hemisphere) were used to infer $\Phi(\alpha_{eq}, E)$. A pitch angle distribution derived from such data is shown in Figure 9 for an energy of 150 keV, i.e., $\Phi(\alpha_{eq}, E=150$ keV). Details of the derivation of the data points A through E in Figure 9 are provided in the appendix. Also shown in Figure 9 are four different near-loss-cone angular distributions that are used to investigate the dependence of the LEP pulse characterisitcs on the pitch angle distribution $g(\alpha_{eq})$, e-folding energy E_0, and the whistler wave intensity. These distributions are marked I, II, III, and IV. The first three distributions I, II, and III are used for investigating the dependence of the LEP pulse features on $g(\alpha_{eq})$ and E_0, whereas profile IV is used to investigate the role of the whistler wave intensity.

The e-folding energy E_0 of the unperturbed electron distribution was estimated to be $E_0 \simeq 120 \pm 40$ keV based on the TE2 detector measurements immediately prior to the LEP burst D. In the following, we show results for $E_0=80$, 120, and 160 keV.

Dependence of LEP Spectra and Pitch Angle Distributions on $g(\alpha_{eq})$ and E_0

In this subsection, we study the dependence of the LEP burst characteristics on the near-loss-cone angular distribution with the use of the three different distributions I, II, and III shown in Figure 9. For all three of these distributions $g(\alpha_{eq}) = 1$ for $\alpha_{eq} > 15.6°$. The equatorial wave magnetic field intensity at 6 kHz is taken to be $B_w = 100$ pT and e-folding energies of $E_0 = 80, 120$, and 160 keV are used as indicated.

Figure 10 shows the results for $E_0 = 120$ keV and for the $g(\alpha_{eq})$ distribution designated I in Figure 9. In the bottom panel we show the computed integral count rate (which would be measured with the TE2 detector) as a function of time, where $t = 0$ is the time at which the whistler wave packet is assumed to enter the magnetosphere at 1000 km altitude. The experimental data points from Figure 2b are superimposed as pluses and are normalized to the same peak value as the computed count rate for convenient comparison of the temporal signature. Since the distributions, I, II, and III do not represent a good fit to the data points in Figure 9, the comparison of the absolute value of the computed peak integral counting rate with data is not useful. Such a comparison is attempted in the next subsection where we use the angular distribution IV to investigate the role of whistler intensity in determining the resultant LEP burst.

The upper panel of Figure 10 shows the computed dynamic energy spectrum, i.e., the variation with time of the energy content of the whistler-induced precipitation pulse, as a three-dimensional plot of differential counting rate (counts/s keV) as a function of energy and time. This plot is to be compared with the measured dynamic spectra of Figure 2.

Figures 11 and 12 employ the formats of Figure 10 and give results for $E_0 = 120$ keV and the $g(\alpha_{eq})$ distributions II and III. Among the three distributions used for comparison, distribution I represents a sharp loss cone edge. For this case particles that are scattered by very small amounts (0.1°– 0.5°) make a substantial contribution to the LEP burst observed by the satellite. As a result the peak counting rate is highest (~ 6000 counts/s) for this case. However, because of
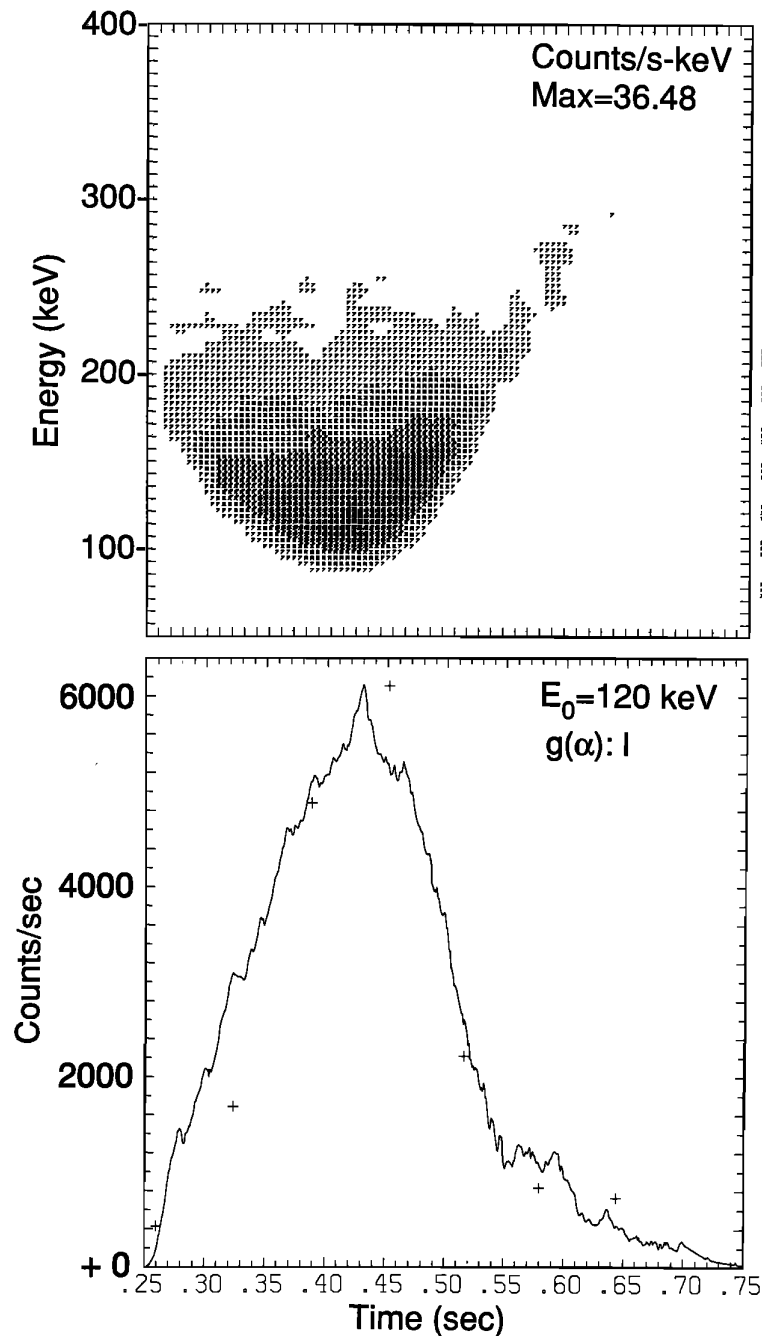
Fig. 10. The curve in the bottom panel shows the computed integral count rate that would be measured by the TE2 detector. The data points from Figure 2b are superimposed as pluses and are normalized to the same peak value as the computed count rate for convenient comparison. The computed curve is for the angular distribution marked I in Figure 9 and for $E_0 = 120$ keV. The whistler wave intensity at 6 kHz was taken to be 100 pT. The top panel gives the computed dynamic energy spectrum of the LEP burst. The intensity of the differential flux is in units of counts/s keV; a scale for the shading is provided on the lower right corner of the panel. The 8 shading levels are equally spaced on a linear scale. The time $t = 0$ represents the time at which the whistler wave enters the magnetosphere at 1000 km altitude at the northern end of the field line.

the large number of particles undergoing small scatterings, those few electrons that are scattered by larger amounts (after the whistler crosses the equator) are relatively unimportant in determining flux levels. The dynamic energy spectrum for the case of distribution I compares less favorably

with the data, having few high-energy electrons at $t > 0.5$ s.

On the other hand, we see that the dynamic energy spectrum for distribution II compares quite well with that measured. This circumstance occurs because distribution II has
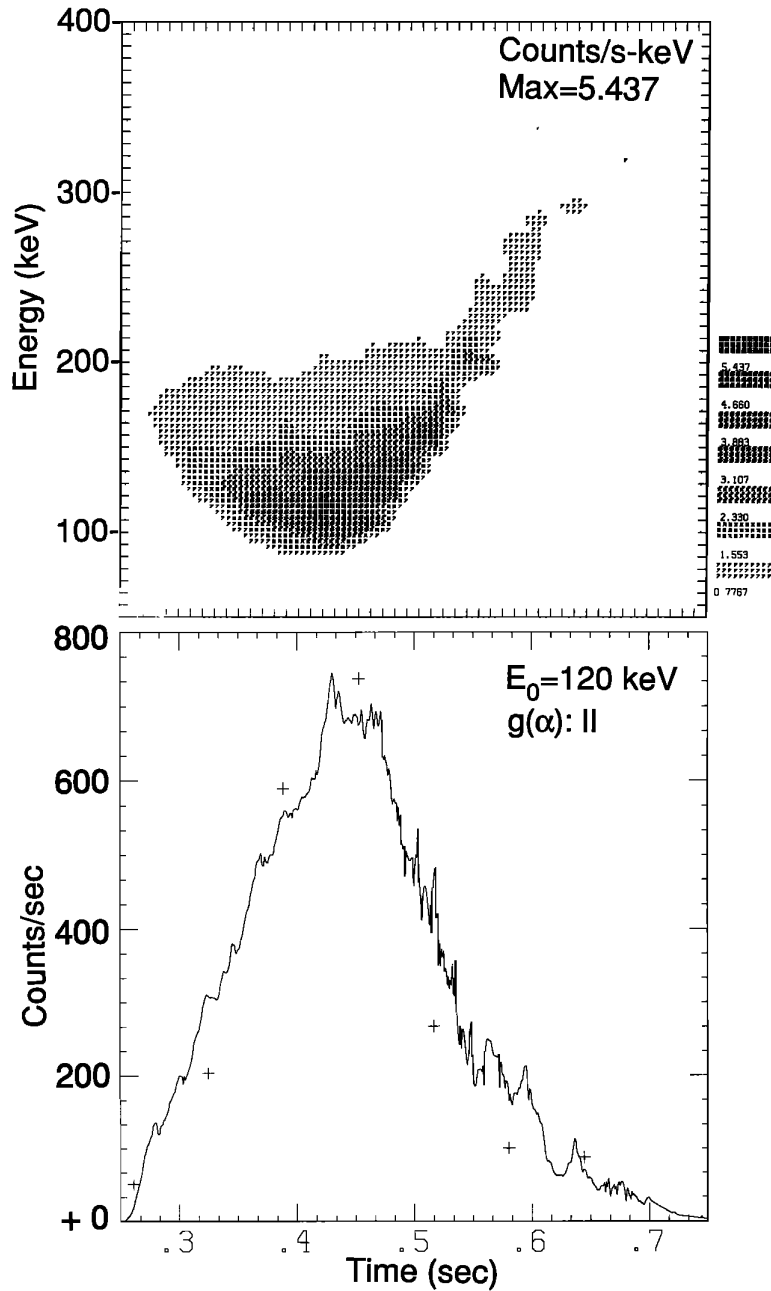
Fig. 11. Results for angular distribution II and for $E_0 = 120$ keV. The format is the same format as Figure 10.

fewer (compared to I) electrons immediately above the loss cone; thus particles that are scattered through small angles constitute a relatively small fraction of the observed LEP burst. For the same reason, those electrons that undergo substantially larger scatterings contribute a greater fraction of the observed flux and in the energy-time signature account for the increasing energy as a function of time. The peak counting rate for distribution II is only ~ 740 counts/s, considerably smaller than that for distribution I, simply due to the reduced number of electrons immediately above the loss cone ($\alpha_{eq} = 14.11°$).

For distribution III the difference in available flux between the two classes of particles (those for which $\Delta\alpha_{eq}$ is small

and those for which it is large) is reduced, and the result is rather similar to that for distribution II, except for the peak counting rate being smaller (~ 440 counts/s). One reason for the difference between the signatures of distributions II and III is that for the parameters of this case most particles undergo scatterings of $\Delta\alpha_{eq} < 1.5°$. Thus the particles contributing to the LEP burst observed on the satellite (observing pitch angles of $\alpha_{eq} < 14.11°$) are mostly those with initial pitch angles of $\alpha_{eq} < 15.6°$. We note, however, that there are few particles (see previous section) which are scattered by larger amounts; their overall contribution for $B_w = 100$ pT is illustrated in the next subsection where we show results for the $g(\alpha_{eq})$ distribution IV.
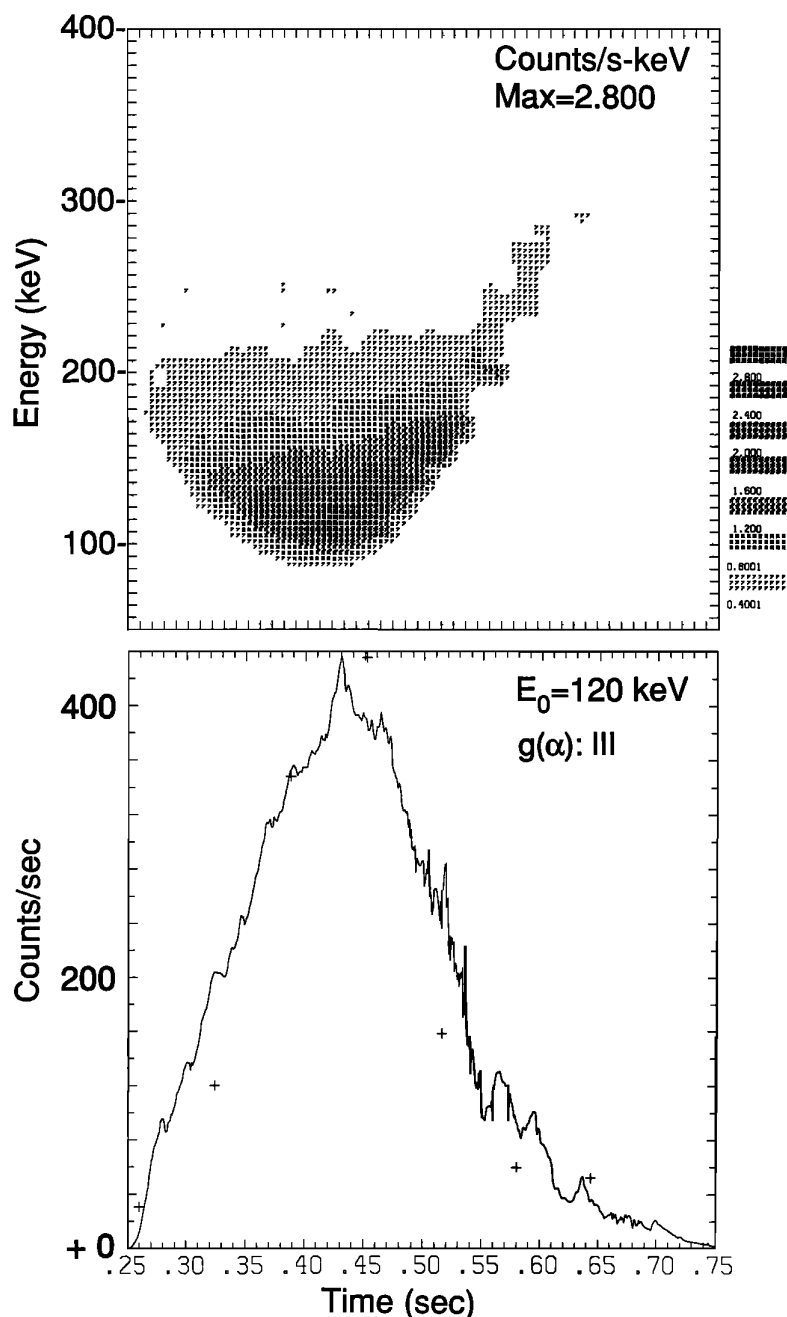
Fig. 12. Results for angular distribution III and for E_0 = 120 keV. The format is the same format as Figure 10.

Figures 13 and 14 have the same format as Figure 10 and show results for distribution II and for E_0 = 80 and 160 keV, respectively. In using the different values for the e-folding energy we have kept the flux level at E = 150 keV constant and equal to 200 el/cm^2 s sr keV. For the case of E_0 = 160 keV, we see from the dynamic spectra that the role of the higher-energy electrons is enhanced compared to E_0 = 120 keV, as expected. Comparing the top panels of Figure 11, 13, and 14 we note that the relative contributions to the LEP pulse of the > 250-keV electrons increases with E_0. Since the data show the contributions of these electrons to be relatively small (see Figure 2, top panel), the predicted

spectrum for E_0 much larger than 160 keV would not be in agreement with the observations.

We conclude from the above arguments that the dynamic energy spectrum of an LEP event is a sensitive indicator of the near-loss-cone pitch angle distribution. The temporal signature of the integral flux does not differ significantly between distributions I, II, and III or with E_0. The absolute peak counting rates do vary substantially with the slope of the pitch angle distribution. Comparison of computed peak counting rate with data is presented in the next subsection.

The computed pitch angle distributions of the LEP pulse for the distributions I, II, and III and for different e-folding
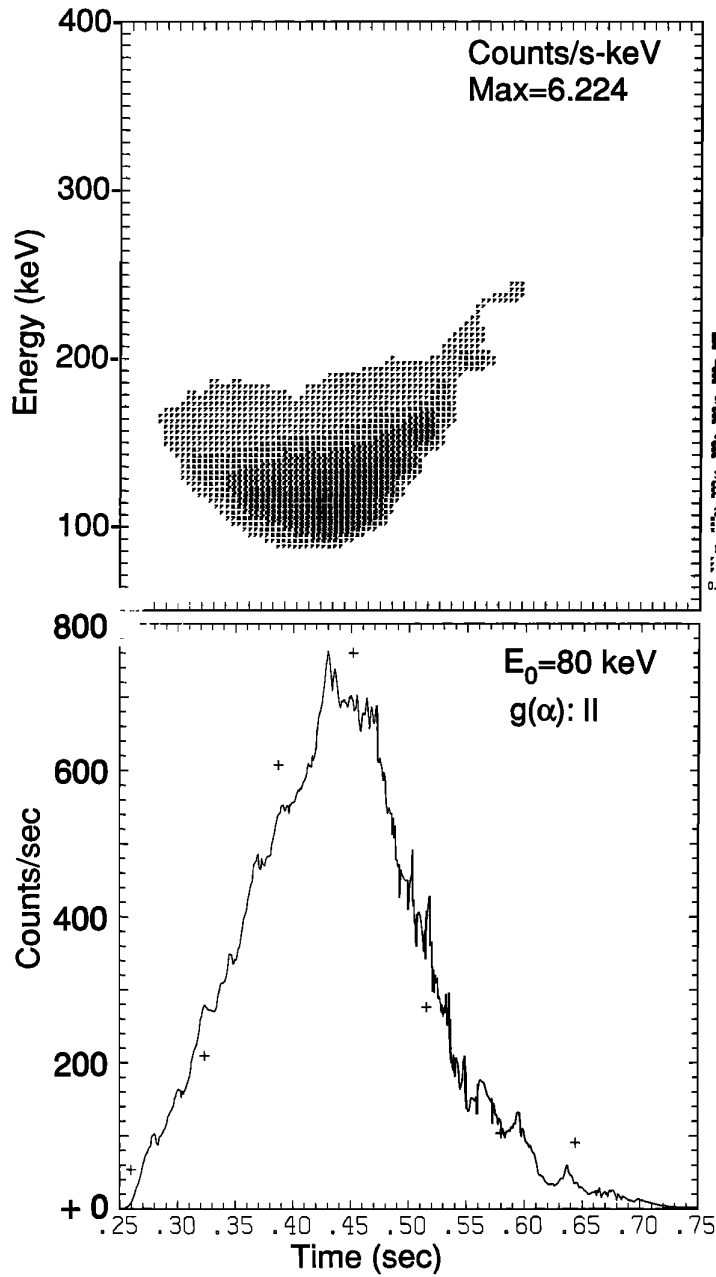
Fig. 13. Results for angular distribution II and for $E_0 = 80$ keV. The format is the same format as Figure 10.

energies (E_0) are shown in Figure 15 and do not exhibit a sensitive dependence on these factors. We note that the pitch angle distribution is somewhat narrower for profile I than for II and III; this result is expected since more particles that can be precipitated with relatively small net scatterings ($\Delta\alpha_{eq}$) are available at the loss cone edge. The pitch angle distribution is found to be slightly broader for E_0=80 keV than for E_0=160 keV; this result is also expected since the particles that undergo relatively large scattering are those with generally smaller energies (i.e., the net scattering for interactions at any point along the field line decreases with increasing energy as shown in section 3).

Comparison of the computed pitch angle distributions

given in Figure 15 with experimental data is difficult since only three electron detectors with relatively wide fields of view were available on the S81-1 satellite. Two detectors labeled TE2 and LE5 had ±20° field of view and their central axes were pointed at pitch angles of 92° and 57°, respectively, during the observations. A third detector labeled ME1 had a field of view of ±30° and was pointed at a pitch angle of 24°. It is not possible to infer the angular distribution of the LEP pulse from the counting rates registered on these three detectors without making assumptions about the general shape of the pitch angle distribution. However, the theoretical distributions can be compared with the data by using the computed profiles to estimate the counting rates
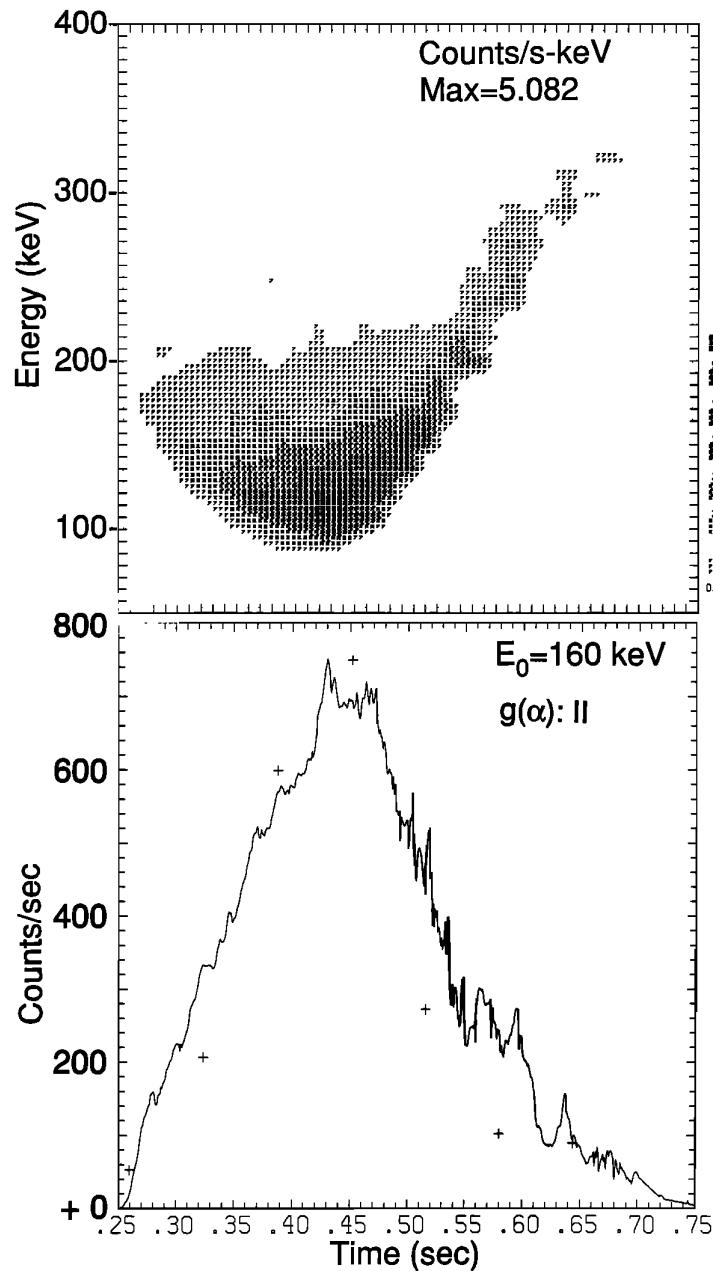
Fig. 14. Results for angular distribution II and for $E_0 = 160$ keV. The format is the same format as Figure 10.

for the different detectors. The results of this analysis are provided in Table 1, where the ratio of the TE2 detector counting rates to those from the ME1 and LE5 detector are shown for LEP pulse pitch angle distributions computed for the $g(\alpha)$ distribution IV, E_0=120 keV, and whistler intensities of B_w=100, 200, and 300 pT. The measured ratios for the first pulse of the LEP event D are also shown for comparison. (The results for $g(\alpha)$ profile IV and B_w=100 pT are also applicable to the case of profile II, since the pitch angle distributions are very nearly the same as can be seen from Figures 15 and 16.) Considering the Table 1 results for B_w=100 pT, we see that the measured counting rate of both the ME1 and LE5 detectors are significantly higher than the computed values, indicating a broader distribution than estimated. The fact that the observed pitch angle dis-

tribution of the LEP pulse was wider (representing deeper penetration into the loss cone) suggests that the intensity of the whistler wave that scattered the electrons may have been larger than 100 pT. In the next subsection, we investigate the dependence of the LEP pulse characteristics on whistler wave intensity.

Dependence of LEP Spectra and Pitch Angle Distributions on Whistler Wave Intensity

In this section we study the role of the whistler wave intensity in determining the properties of the LEP pulse, namely, the temporal variation of the integral flux, the dynamic energy spectra, and the pitch angle distribution. For this purpose we assume the pitch angle distribution of the

TABLE 1. Counting Rate Ratios for TE2, LE5
and ME1 Detectors

	$\dfrac{\text{TE2}(92^\circ)}{\text{LE5}(57^\circ)}$	$\dfrac{\text{TE2}(92^\circ)}{\text{ME1}(24^\circ)}$
Experimental values	6.6	10
Values computed using test particle model		
$B_w = 100\text{pT}$	52	infinite
$B_w = 200\text{pT}$	21	1900
$B_w = 300\text{pT}$	12	89

Numbers in parentheses denote angle between detector axis and magnetic field.

trapped electrons in the vicinity of the loss cone to be the distribution IV of Figure 9 and the e-folding energy of the trapped distribution to be E_0=120 keV. This distribution provides a reasonable fit to the data points derived from S81-1 measurements in the southern hemisphere and shown as the filled circles in the same figure (see appendix).

The results of the model computation for three different wave intensities of B_w = 100, 200, and 300 pT are shown in Figures 16, 17, and 18, respectively. The top panels show the dynamic energy spectra, the middle panels show the integral
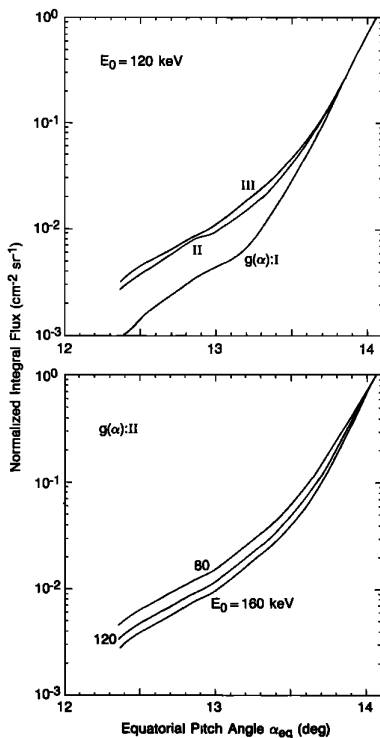

Fig. 15. The computed pitch angle distributions of the LEP pulse integrated over both time and energy are normalized to unity at α_{eq} = 14.1°. The top panel shows results for E_0 = 120 keV and $g(\alpha)$ profiles I, II, and III, whereas the bottom panel shows the distributions for $g(\alpha)$ profile II and E_0 =80, 120, and 160 keV. In both cases whistler wave intensity at 6 kHz was taken to be B_w=100 pT.
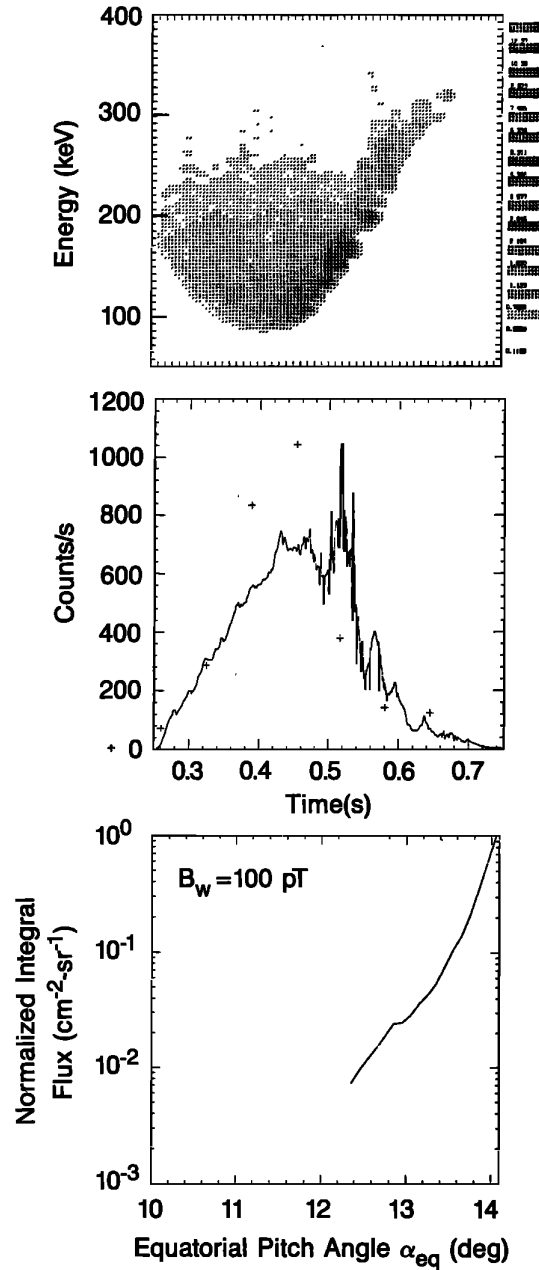

Fig. 16. Model results for whistler intensity of 100 pT, E_0=120 keV, and $g(\alpha)$ profile IV. The top panel shows the computed dynamic energy spectra of the LEP burst. The intensity of the differential electron flux is in units of counts/s keV; a scale for the shading is provided on the right edge of the plot. The 15 shading levels are equally spaced on a logarithmic scale. The middle panel shows the computed integral counting rate that would be measured by the TE2 detector. The data points from Figure 2b are superimposed as pluses and are normalized to the same peak value as the computed count rate for convienent comparison. The lower panel shows the pitch angle distribution of the LEP pulse integrated over both time and energy and normalized to unity at the pitch angle of α_{eq} = 14.1°. The time t = 0 is the time of entry of the whistler wave packet into the magnetosphere at 1000 km altitude.

counting rates as a function of time, and the bottom panel shows the pitch angle distributions integrated over both time and energy.

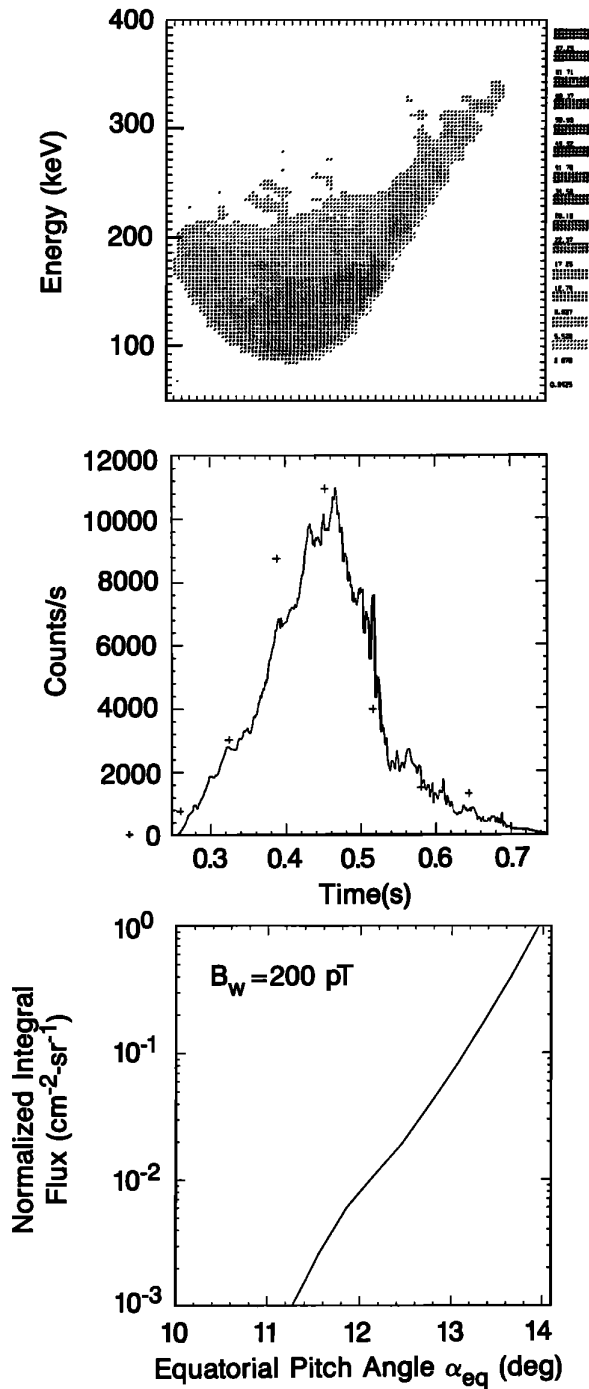A comparison of the results for B_w = 100 pT in Fig-

due to those electrons that have undergone relatively larger pitch angle scatterings ($\Delta\alpha_{eq} > 0.8°$). The relative contributions to the integral flux by particles scattered by such large $\Delta\alpha_{eq}$ compared with those that have suffered smaller scatterings as represented by distribution IV is not consistent with data for $B_w = 100$ pT on the basis of the temporal profile of the integral counting rate.

Since distribution IV represents a reasonable fit to the data points extracted from the satellite measurements (see Figure 9), we can compare the measured and computed LEP

Fig. 17. Model results for whistler wave intensity of 200 pT, E_0=120 keV, and angular distribution for trapped electrons as given by of $g(\alpha)$ profile IV. The format of the figure is identical to that of Figure 16.

ure 16 with the results presented in Figures 11–15 further illustrates the role of the near loss cone trapped electron distribution $g(\alpha)$. For example, consider the result for distribution II as shown in Figure 11 and that for distribution IV given in Figure 16. The higher fluxes of particles at $\alpha_{eq} > 15°$ has introduced a secondary peak (at ~ 0.5 s in Figure 16, middle panel) in the integral counting rate profile
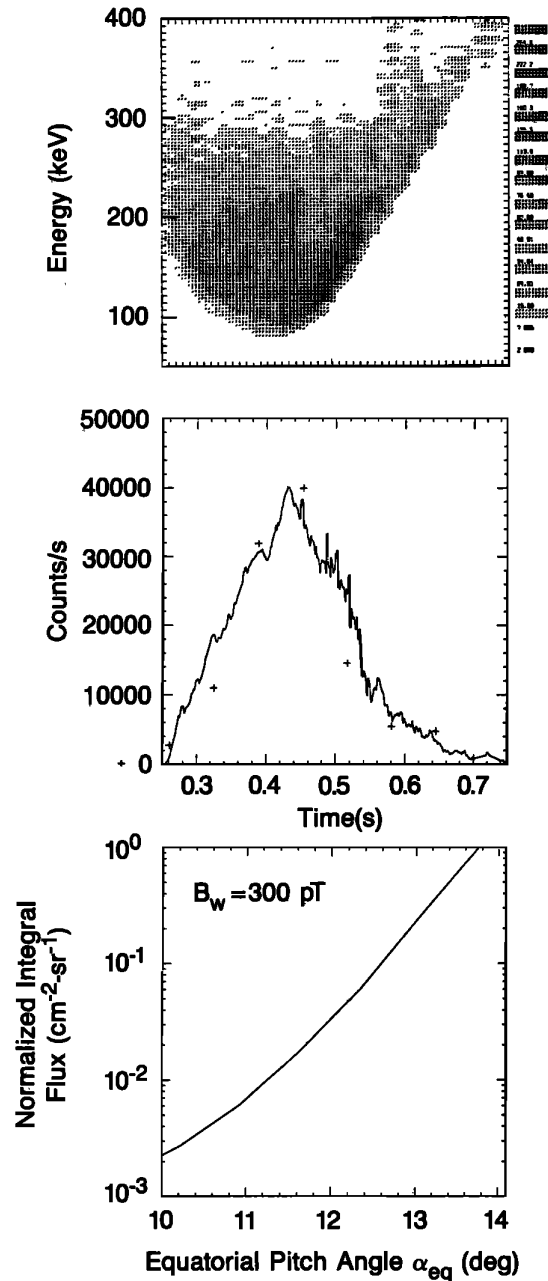
Fig. 18. Model results for whistler wave intensity of 300 pT, E_0=120 keV, and angular distribution for trapped electrons as given by $g(\alpha)$ profile IV. The format of the figure is identical to that of Figure 16.

pulses in terms of the absolute value of the peak integral counting rate. The peak counting rate for event D as measured on the TE2 detector and shown in Figure 2 is $\sim$ 9500 counts/s, whereas the model estimate for $B_w = 100$ pT is $\sim$ 1000 counts/s, clearly not consistent with the data.

The pitch angle distribution of the LEP pulse for $B_w = 100$ pT and profile IV is not very different from those for profiles I, II, or III as shown in Figure 15. The comparison of the relative counting rates to be observed by the different detectors for this case is given in Table 1; results are very similar to those for $g(\alpha)$ profile II that were discussed above. The computed pitch angle distribution is narrower than the measured one as is indicated by the significantly smaller fluxes predicted for the ME1 and LE5 detectors.

Results for $B_w = 200$ pT and 300 pT are given in Figures 17 and 18. Comparing with the data shown in Figure 2, we find that the model prediction for 300 pT overestimates the peak integral counting rate. Furthermore, the dynamic energy spectrum for $B_w = 300$ pT is noticeably different from the measured one (Figure 2); specifically, the initial part of the computed LEP pulse consists of a wider range of particles. The model predictions for $B_w = 200$ pT are in good agreement with the data in a number of respects. The temporal profile of the integral counts provides a better fit to the data points than those for 100 pT or 300 pT. The computed peak integral counting rate is $\sim$ 11000 counts/s, which is within 15% of the measured peak of $\sim$ 9500 counts/s. Furthermore, the dynamic energy spectra of the computed LEP pulse for $B_w = 200$ pT are closest to that measured (Figure 2).

For the parameters used here, the whistler-particle scattering process is inherently linear in the sense that the net scattering $\sqrt{< (\Delta\alpha_{eq})^2 >}$ for any group of particles is approximately proportional to the whistler intensity B_w [Inan et al., 1987]. On the other hand, it is clear from the results of Figures 16, 17, and 18 that dependence of the counting rate of the LEP pulse on whistler intensity is highly nonlinear. This result is due primarily to the initial pitch angle distribution which represents a nonlinear weighting function for particles at different pitch angles. Increasing the wave intensity makes it possible for particles at higher pitch angles to be scattered to $\alpha_{eq} < 14.1°$ (and to be observed on the SEEP satellite) and in view of the particle distribution the number of available electrons increases exponentially with pitch angle.

In terms of the pitch angle distribution, we note from Table 1 that the counting rate estimated for the LE5 detector is within a factor of $\sim$ 3 and of $\sim$ 2 that measured respectively for $B_w = 200$ and 300 pT. The predicted counting rates for the ME1 detector are considerable smaller than measured; however, it is important to note that this detector intercepted electrons only at the extreme edge of its angular sensitivity during the LEP event D. The comparison with the data from the LE5 detector is not subject to such uncertainty and thus the discrepancy between the computed and measured ratios as given in Table 1 indicates that the LEP pulse pitch angle distribution is indeed broader than that which is allowed by the simple model. Since the computed and measured integral counting rates as well as the dynamic energy spectra are in agreement for B_w=200 pT, it appears that the number of electrons scattered by the whistler are as predicted by the model; however, the pitch angles of some electrons appear to have been deflected further than expected. This result and its implications are further discussed in the following section.

5. LATITUDE EXTENT OF THE SCATTERING REGION

The comparison of the model results with data as presented above indicates that the test particle model can accurately account for many of the observable aspects of the LEP pulse. In this section, we employ the model to identify the contributions to the LEP pulse from whistler-particle interactions occurring in different regions along the field line.

The single particle results presented in section 3 show that the maximum scattering by a given whistler does not occur at the equator. To investigate the relative contributions to the resultant LEP burst from interactions occurring in different regions, we compute whistler-induced flux signatures that would result if the interaction were limited to narrow latitude ranges ($\lambda_0 \pm 2.5°$) centered at different points (λ_0) along the field line. The range of $\pm 2.5°$ was chosen since typical interaction lengths for most particles are $< 5°$ in latitude as was shown in the previous section. Limiting the interaction to such narrow ranges is achieved by imposing a whistler wave intensity of $B_w = 0$ outside the region of interest. In this way all of the wave and particle kinematics are retained, and the results can be directly compared to the full-interaction results presented above.

Dynamic Energy Spectra and Integral Counting Rates

Results of the test particle simulation for different λ_0 are shown in Figure 19. Here we show results for $\lambda_0 = 15°, 10°, 5°, 0°, -5°, -10°, -15°$, in plots marked A-G, respectively, each of which have the same format as Figure 10. For all cases we have used the $g(\alpha_{eq})$ distribution II (Figure 9) and an e-folding energy of $E_0 = 120$ keV. The results for these parameters and for the complete interaction (Figure 11) are repeated at the upper left corner of Figure 19 for easy comparison. Note that linear superposition of the dynamic spectra or the integral counting rate for regions A through G will not give a result equal to that computed for the complete interaction case. This difference is due to the fact that when the interaction is artificially limited to a region of $\lambda_0 \pm 2.5°$ some individual particle trajectories are interrupted in the middle of the resonant interaction, resulting in different net scattering $\Delta\alpha_{eq}$ than would have occurred with the full interaction. Since the whistler-particle interaction involves a spatially distributed interaction (see Figures 4-7), it is not possible to decompose the interaction into separate spatial regions that, when summed together, would produce the complete interaction. Nevertheless, the decomposition presented in Figure 19 is useful for conceptual illustration of the relative contributions from interactions occurring at different locations.

Considering first the equatorial interaction region(marked D) for $\lambda_0 = 0°$, we see that the LEP pulse signatures are significantly different in a number of aspects from those measured. First, the onset time of the predicted integral count rate is delayed by as much as $\sim$ 100 ms with respect to the data points (pluses) indicating that the initial part of the LEP burst is due to those particles that encounter the wave before it arrives within $\sim$ 2.5° of the geomagnetic equator. The same result is even more evident in the dynamic spectrum. The initial electron flux that is apparent in both the data (Figure 2) and the computed spectrum for the full-
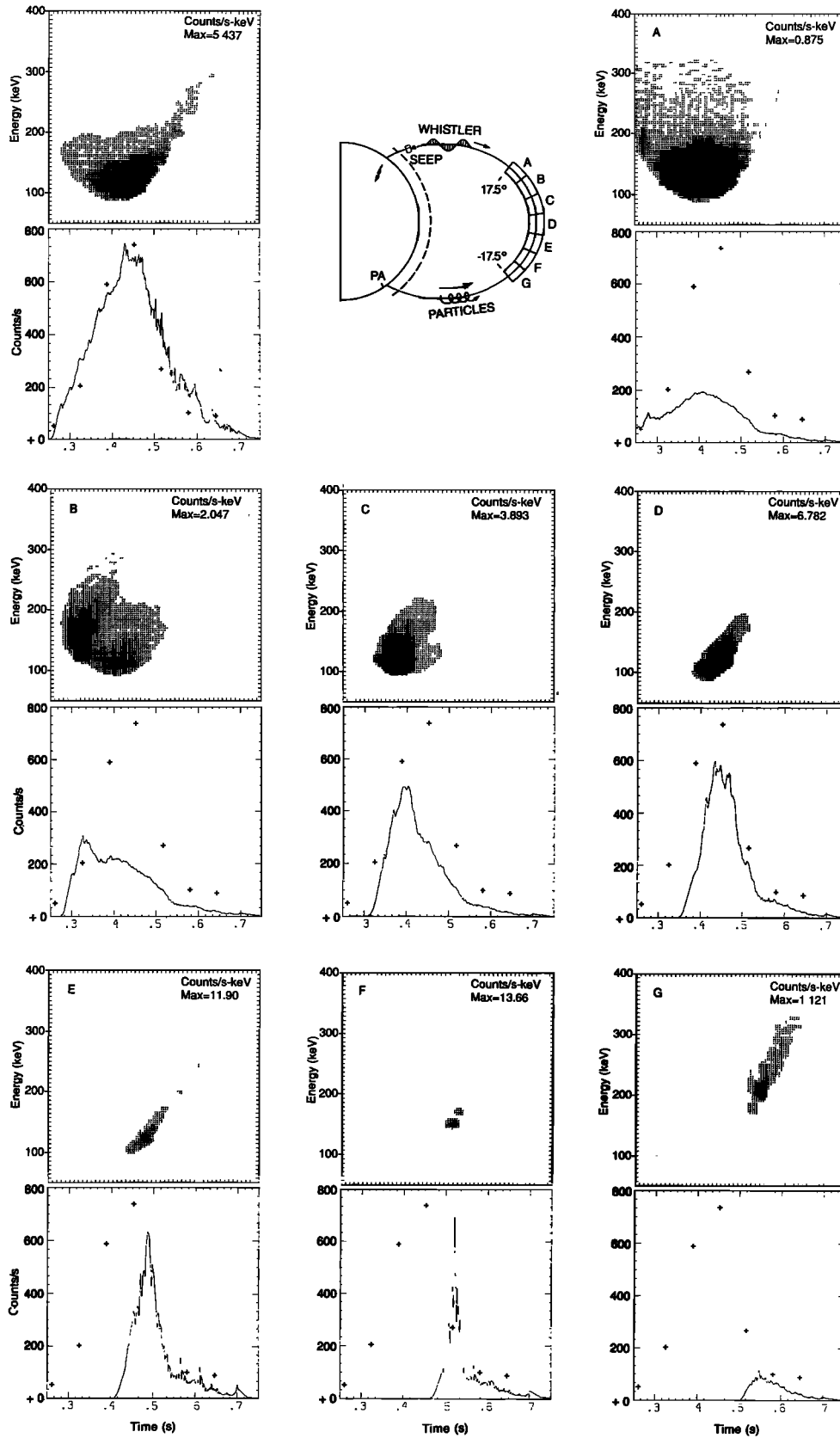
Fig. 19. Computed dynamic energy spectra and integral counting rates for whistler intensity of 100 pT, angular distribution II and for $E_0 = 120$ keV with the whistler-particle interaction limited to different regions of $5°$ width in latitude and centered at $\lambda_0 = 15°, 10°, 5°, 0°, -5°, -10°, -15°$ (A, B, C, D, E, F, G, respectively). The results for the case full interaction occurring throughout the field line were given in Figure 11 and are reproduced in the upper left panel.

interaction case is not present, indicating that this feature is a signature of interactions occurring before the whistler wave packet reaches the vicinity of the equator. A second point is the lack of any significant contribution to the LEP pulse from particles with energies $E > \sim 200$ keV, as is apparent from the dynamic spectrum. This result is consistent with the results of the previous section, where it is shown that such particles, interacting with the wave after the wave front crosses the equator, undergo maximum scattering at latitudes of $5° - 10°$ away from the equator. The absence of the contributions of these particles is also apparent in the peak integral count rate of the LEP burst, which is ~ 600 counts/s for the equatorially limited interaction case as opposed to ~ 740 counts/s for the full interaction case.

Panels A, B, and C of Figure 19 illustrate that the initial part of the observed dynamic spectra originates in interactions which occur before the wave arrives at the equator. The effect of the relatively large scatterings resulting from the second-order resonances discussed in the previous section is seen in panels D and F; particles in a relatively narrow energy range produce large peak fluxes. Contributions from segment F are considerably smaller in magnitude but constitute the latest arriving higher-energy component of the LEP pulse.

In terms of the extent of the scattering region along the field line, the above analysis indicates that the majority of the electrons constituting the observed LEP pulse are scattered by the whistler wave in the latitude range of $\sim 20°$ N to $\sim 20°$ S. On the basis of the test particle calculations, the contributions to the LEP pulse from regions outside this range are relatively small. Successful reproduction with the same model of most of the features of the LEP pulse measured on September 9, 1982, suggests that the primary causative mechanism is a high-altitude whistler-particle gyroresonant interaction.

The results of Figure 19 illustrate that the overall effects of interactions occurring at points distributed along the field line determine the temporal signature of the counting rate as well as the dynamic energy spectrum. This circumstance is to be expected, since the whistler wave packet contains a wide range of frequency components. At the wave front the higher-frequency components interact with relatively low energy particles away from the equator; however, as the wave packet moves closer to the equator, these low-energy electrons can now interact with lower-frequency components. The former and latter interactions can be equally effective in terms of pitch angle scattering, thus accounting for the nearly constant energy initial portion of the dynamic energy spectrum shown in Figure 2. Another factor to be considered is the available trapped flux at different energies. Thus for an e-folding energy of $\sim$120 keV, less efficient scattering of lower-energy particles can produce approximately the same integral counting rate as more efficient scattering of higher-energy particles.

Pitch Angle Distributions

The pitch angle distributions predicted to result for interactions occurring in different regions along the field line are shown in Figure 20. At the upper left corner is given the normalized pitch angle distribution integrated over the duration of the LEP pulse as well as over energy for the case of $E_0 = 120$ keV and the initial pitch angle distribution II. We

see that the penetration into the loss cone is $\sim 1°$, with the relative flux at $\alpha_{eq} = 13°$ being a factor of $\sim 10^2$ lower than that at the edge of the loss cone ($\alpha_{eq} = 14°$). This result is generally consistent with the individual particle scatterings presented in section 3 above, where it was shown that most particles experienced a net scattering of $\sim 0.1°$ to $1°$. Some particles were scattered by $> 1°$ (see Figure 5); however, the contribution to the overall flux of these few particles is relatively low. The remaining panels of Figure 20 show the pitch angle distribution that would result if the interaction were limited to $5°$ latitude ranges centered at different locations along the field line. The result illustrates the aspects of the whistler-particle scattering process that were discussed in section 3 and in connection with Figure 19. The pitch angle distribution broadens as the interaction location approaches (A, B, C) and crosses (D, E) the equator. The loss cone penetration is greatest for interactions in region F, consistent with the results of section 3, showing that the largest individual particle scatterings occur at latitudes of $\sim 10°$S. Interactions occurring past region F, for example, in region G, produce less pitch angle scattering, and the distribution is accordingly narrower as shown in Figure 20.

The variation of the pitch angle distribution with latitude of the interaction region as shown in Figure 20 would result in a corresponding variation with time of the distribution observed at the low altitude satellite. (Note that the arrival time and flux contribution from each segment are shown in Figure 19.) During a short (~ 300 ms) LEP pulse the pitch angle distribution would be expected first to broaden with time, being widest shortly after the peak of the LEP pulse, and subsequently to become narrow again toward the tail of the pulse. Such features of LEP bursts have to date not been observed, and the results presented in Figure 20 represent a theoretical prediction concerning the dynamic variation of the pitch angle distribution of an LEP pulse. The experimental measurement of this quantity would consititute a new diagnostic tool for determining the latitudinal extent of the "effective" wave-particle scattering region along the field line. In order to be useful for comparison with the theoretical predictions, such measurements must be made with high resolution in pitch angle ($\sim 0.5°$ resolution in equatorial pitch angle or $\sim 10°$ resolution in local pitch angle at low altitude). Furthermore, very high instrument sensitivity is needed in order to measure the dynamic variation of the pitch angle distribution over the duration of the LEP pulse (~ 300 ms).

6. DISCUSSION

Whistler Wave Intensity

The comparison of the measurements with the data as discussed above suggests that the whistler equatorial magnetic field intensities at 6 kHz may have been ~ 200 pT. Most estimates of equatorial field strength of ducted whistlers, based upon ground observations, lead to values that do not exceed 100 pT. Such is also the case for the whistlers observed at Palmer on September 9, 1982. To estimate the equatorial intensities one must take into account spreading losses and the waveguide attenuation between ionospheric exit points and the receiver. If these losses are reasonably well known, estimates of the equatorial strength based upon the stronger ground whistlers received from time to time should agree with one another within perhaps a few deci-
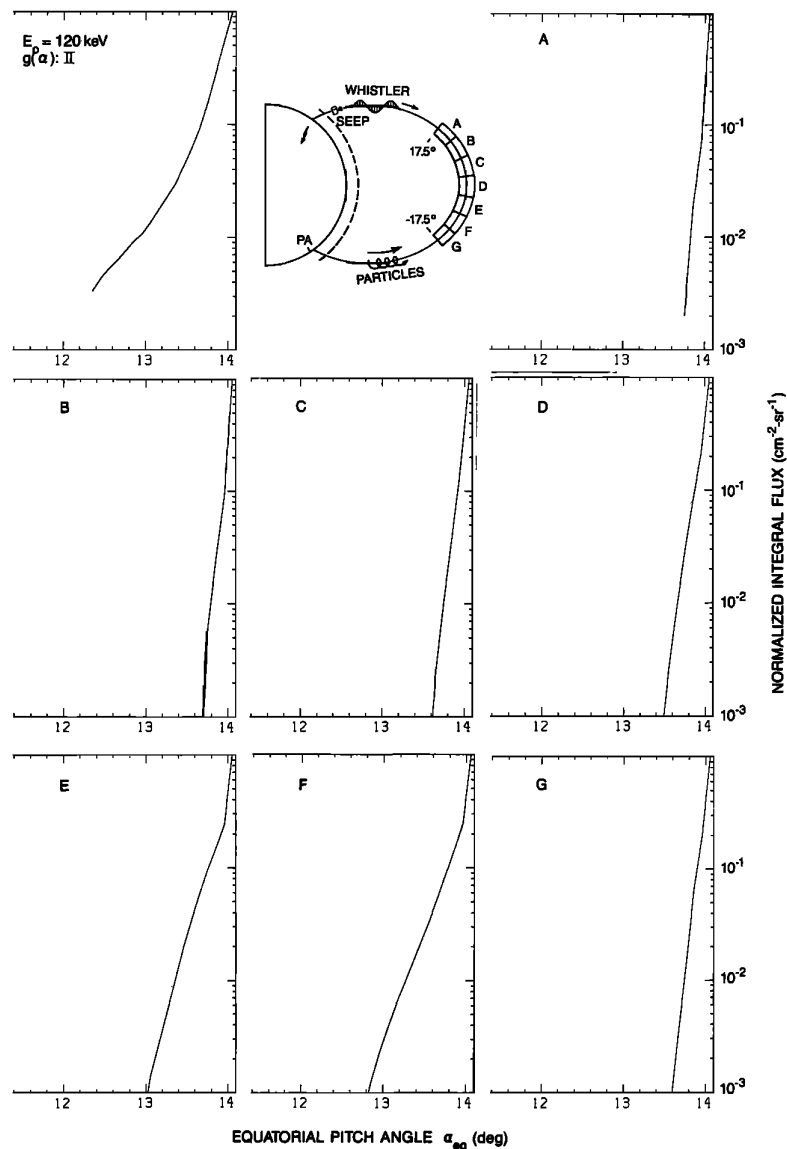
Fig. 20. The pitch angle distribution of the LEP pulse as computed with the test particle model for 100 pT whistler wave intensity, angular distribution II, and for $E_0 = 120$ keV. In panels A-G the whistler-particle interaction was limited to different regions of $5°$ width in latitude and centered at $\lambda_0 = 15°, 10°, 5°, 0°, -5°, -10°, -15°$, respectively. The upper left panel is the distribution for the case when interaction occurred throughout the field line.

bels. However, the spreading losses are large, ~ 7 dB/100 km [Tsuruda et al., 1982], and uncertainties in that loss, in addition to uncertainties in exit point location, may obscure the occasional existence of equatorial fields larger than 100 pT. For example, Helliwell [1965] reports the observation near $L = 2$ of a whistler with field strength at the receiver of about 5 mV/m. Applying the usual waveguide attenuation and spreading losses to this case leads to an estimate of an equatorial field of ~500 pT.

The pitch angle scattering in the magnetosphere might have been caused by other wave components (such as nonducted whistlers) launched by the same lightning discharge. That the LEP bursts observed on September 9, 1982, might have been induced by nonducted whistlers was pointed out [Voss et al., 1984] on the basis of the spatial extent of the

region (~ 500 km) traversed by the satellite. As a result of possible focusing of ray paths the whistler wave intensity in the magnetosphere can be higher for nonducted waves. However, a conclusive assessment cannot be made in the absence of in situ wave measurements. Whistlers are commonly observed on high-altitude satellites such as ISEE 1 and DE 1 near the equatorial plane; however, no comprehensive quantitative study has yet been made of the distribution of whistler wave intensities. On the basis of selected cases studied so far, magnetic field amplitudes in excess of 100 pT are not typical.

Other observations on September 9, 1982, support the contention that relatively large whistler wave fields could have been present on the SEEP field lines. Whistlers generally similar to the Palmer events were seen at Siple Station,

Antarctica (76°S, 84°W) and Roberval, Quebec (48.4°N, 72.3°W), about 3 hours earlier and exhibited multihop echoing. On the ISIS 2 satellite in the southern hemisphere at 1400 km altitude at $L \sim 2.2$ and 13° in longitude west of Palmer, very strong one-hop whistlers were observed 1.5 hours after the SEEP pass. Third and fifth hop echoes appeared. The first hop contained multiple components, suggesting ducted propagation prior to reception at the satellite. Considering that a large magnetic storm occurred on September 6 and 7 and that Kp rose to 7^- in the first 3 hours on September 9, it is plausible that particle fluxes during the SEEP pass were relatively high and that conditions were good for whistler amplification in the several kHz range. That the ground station at Palmer did not detect strong, well-defined whistlers during the SEEP pass could well be due to ionospheric absorption or reflection of downcoming waves.

The fact that the better-defined whistlers observed at Palmer on September 9, 1982, were associated with the smaller electron fluxes on SEEP suggests that the lightning flashes were distributed in longitude. Those flashes closer to the SEEP path give rise to the larger particle bursts and therefore (due to increased distance from the whistler path entrance points) to the weaker whistlers. We note here that event D was one of the three strongest LEP bursts. Other LEP bursts observed during the same period, such as event F shown in Figure 1, have lower peak values (by a factor of ~ 100). However, we note from Figure 1 that the whistler associated with event F measured at Palmer station is significantly stronger than that of event D (amplitude measurements show a factor of ~ 5 larger intensity at 1.5 kHz). Thus it is possible that the causative lightning flash for event F was closer to the field line leading to Palmer station and further from the field line passing through the satellite location. Assuming the intensity of the lightning stroke to be the same, the whistler wave intensity on the field lines of the satellite for event F would be lower, thus accounting for the lower observed fluxes. In the absence of any measurement of the lightning intensity and location, other explanations can also be envisioned; it is possible, for example, that the lightning stroke associated with event D was unusually intense. The same condition must then be the case for events A and E.

Comparison With Previous Work

In a recent paper, Goldberg et al. [1987] report observations of two LEP events. Their spectral analysis was based on the time interval between the lightning flash, the arrival of the first electron pulse, and the arrival of the echoing pulse of electrons backscattered from the southern hemisphere. From these data they conclude that the energies of initial electrons in the pulse were centered near 100 keV but extended above 200 keV, in general agreement with our results. They also observed additional structure in the time profile for the first 0.3 s and attributed the first maxima to the mechanism discussed here and the subsequent structure to processes not yet identified. No such secondary peaks were observed in our measurements, and although the time resolution of Goldberg et al. was superior (0.01 s versus 0.064 s), we would have resolved similar structure had it been present. An additional discrepancy with Goldberg et al. is found in the relative amplitudes of the initial pulse

and the first echo. When viewed at small pitch angles, we find the second peak (first echo) is always larger than the initial precipitating electron burst, [Voss et al., 1984] a condition resulting from the broader angular distribution of the echoing electron bunch. In the Goldberg cases the first peak was a factor of 2 larger than the first echo, and subsequent echoes were not observed. These discrepancies may be caused by differences in the energy and angular response of the two experiments, by differences in the altitudes at which the instruments were located, or by individual variations in the LEP events. In Figure 1 the various events have somewhat different time traces; only a well-separated whistler such as event D produced the idealized profile with 5 or 6 well-defined echoes.

Pitch Angle Distribution of the LEP Pulse

An important and puzzling result of our comparison of experimental data with model predictions was the finding that the pitch angle distribution of the LEP pulse computed with the model did not agree well with the relative counting rates registered by the different detectors on the SEEP satellite. Specifically, the counting rate computed for a whistler wave intensity of $B_w = 200$ pT for the LE5 detector (pointed at 57° with respect to the magnetic field) was a factor of ~ 3 lower than the measured value. The apparent agreement between theory and data in terms of peak integral counting rate and dynamic energy for the same whistler intensity indicates that the discrepancy in pitch angle distribution cannot simply be attributed to the strength of the scattering wave field. The number of electrons scattered by the whistler and their energy spectrum as it varies over the duration of the LEP pulse are as predicted by the model. However, the pitch angles of individual electrons appear to have been deflected further than expected.

While further comparison of LEP event pitch angle distributions predicted by the model with data must await measurements with higher pitch angle resolution, the discrepancy mentioned above cannot be attributed to uncertainties in the detector angular response or pointing accuracy. To confirm the detector response and pointing accuracy in orbit, we have analyzed the counting rate ratios of the TE2 and LE5 detectors for the five southern hemisphere passes discussed in connection with Figure 9 (also see appendix). Using the pitch angle distributions for trapped electrons at these locations (dashed lines in Figure 9), the TE2 to LE5 counting rate ratios were estimated to be greater than ~ 250, in good agreement with measured values.

One possible explanation for a broader than expected LEP pulse pitch angle distribution would involve irregularities in cold plasma density along the magnetic field line. Deviations from the assumed smooth diffusive equilibrium model would have the tendency to enhance the latitudinal extent of resonance regions for some particles while decreasing it for others. Such a circumstance would not lead to an increase in the number of particles scattered by the wave; hence the integral counting rates would remain the same. However, since some particles would have been scattered by larger amounts a broader pitch angle distribution would result. Another possible explanation involves the nonducted nature of whistler waves that was discussed above in connection with whistler field intensity. Nonducted waves have a broader wavelength spectrum which might map into a

broader distribution of scattering angles. Detailed assessments of these suggestions and other possible explanations for the discrepancy require further study.

7. Summary and Conclusions

The analysis of the LEP event observations on September 9, 1982, using a test particle model of the whistler-particle interaction indicates the following:

1. The dynamic energy spectra of the LEP pulse and the temporal profile of the integral counting rate are consistent with the predictions of a test particle model of the gyroresonant scattering of the electrons by a whistler wave having an equatorial intensity at 6 kHz of ~ 200 pT.

2. The measured LEP pulse pitch angle distribution is wider than that estimated on the basis of the test particle model.

3. The dynamic energy spectra of the whistler–induced precipitation flux depends sensitively on the details of the particle pitch angle distribution near the loss cone.

4. The LEP pulse consists of particles interacting with the whistler wave over a range of latitudes; interactions occurring before and after the wave front crosses the equator have identifiable signatures in the dynamic energy spectrum. For the parameters considered here, maximum scattering is experienced by particles interacting with the whistler after it has crossed the equator and reached a latitude of $\sim 10°$ S. However, scattering occurring in other regions is significant, and the cumulative effects of interactions at points distributed along the field line need to be considered for an accurate determination of the dynamic energy spectrum and temporal signature of LEP events. For event D of Figure 1, the observed LEP pulse consisted mostly of electrons scattered in the magnetic latitude range of $20°$ N to $20°$ S.

5. The pitch angle distribution of lightning-induced electron precipitation is computed in terms of its expected variation during an LEP pulse. As observed on a low-altitude satellite, the distribution is expected to first broaden with time, being widest shortly after the peak of the pulse and subsequently becoming narrow toward the tail of the LEP pulse.

In view of the many assumptions involved in modeling the whistler-induced precipitation of energetic radiation belt particles, results obtained by the application of a relatively crude model to the SEEP data are encouraging. However, further study of LEP events are needed to further our understanding of lightning-induced electron precipitation phenomena and their contribution to the loss rates of energetic radiation belt particles.

Appendix: Estimation of the Electron Pitch Angle Distribution Near the Loss Cone

In the region where the LEP events were observed, the S81-1 satellite was in the northern hemisphere, and the position in the southern hemisphere conjugate to the satellite was below sea level. Therefore during these events the satellite was not able to observe trapped electrons. However, during the southern hemisphere passes trapped electrons were measured and these fluxes were used to estimate the population of trapped particles.

In two southern hemisphere passes immediately before the

TABLE A1. $L = 2.3$ Crossings for Figure 9

Pass	Latitude deg	Longitude deg	B field gauss
A	−58.8	− 40.0	0.300
B	−61.3	− 60.9	0.334
C	−60.95	− 83.3	0.373
D	−57.59	−107.2	0.417
E	−52.47	−131.5	0.452

LEP events and three passes after the LEP observations the counting rates of the TE2 detector were observed at $L = 2.23$. The geographic longitude and latitude and the local magnetic field values at these five measurement locations are tabulated in Table A1. At these times the detector axis was oriented at angles between $95.3°$ and $109.3°$ to the local magnetic field. From these data the pitch angle distribution of the source population for the LEP events was derived by the following procedure.

High-resolution pitch angle distributions in this region of the magnetosphere were measured previously on the P78-1 satellite [Imhof et al., 1986]. This satellite was in a polar orbit at 600 km altitude and was equipped with a detector having a $3°$ acceptance angle. During each 6-s spin a complete angular distribution was observed. These angular distributions taken in the southern hemisphere near the longitude of the SEEP passes were transformed to 230 km altitude and were assumed to be typical of those encountered by the SEEP satellite. These distributions were then normalized to give the counting rates observed on SEEP during the five passes, each pass being at a different longitude and therefore at a different magnetic field value as tabulated in Table A1. The relationship of counting rate, detector geometric factor, and electron angular distribution is discussed elsewhere [Voss et al., 1988, manuscript in preparation].

These normalized angular distributions for the southern hemisphere passes were transformed to the equatorial plane and are plotted as the five dashed curve segments in Figure 18. Each curve was taken at a different longitude and therefore at a different B value, the curves on the right of the figure being at more easterly longitudes. In this region of the magnetosphere as one moves eastward at constant altitude and L value, the magnetic field decreases and the equatorial pitch angle of the mirroring electrons increases. Each curve of the five samples includes only those equatorial pitch angles accessible at 230 km altitude, but since each pass was made at a different magnetic field value, the five passes cover the range of equatorial pitch angles from $13.9°$ to $17.8°$.

The most appropriate curve to represent the distribution near the loss cone is one which best fits the uppermost point of each of the five curve segments. This highest value represents electrons mirroring at 230 km, which is significantly above the Earth's atmosphere. Other points on each curve segment represent local pitch angles less than $90°$ and correspond to electrons mirroring below 230 km. It is expected that these electron fluxes have been reduced by collisions with the atmosphere as they experience eastward drift towards lower mirroring points.

REFERENCES

Angerami, J. J., and J. O.Thomas, Studies of planetary atmospheres, 1. The distribution of electrons and ions in the earth's exosphere, *J. Geophys. Res., 69*, 4537, 1964.

Carlson, C. R., R. A. Helliwell, and D. L. Carpenter, Variable frequency VLF signals in the magnetosphere: Associated phenomena and plasma diagnostics, *J. Geophys. Res., 90*, 1507, 1985.

Carpenter, D. L., and U. S. Inan, Seasonal, latitudinal and diurnal distributions of whistler-induced particle precipitation events, *J. Geophys. Res., 92*, 3429, 1987.

Carpenter, D. L., and J. W. LaBelle, A study of whistlers correlated with bursts of electron precipitation near $L = 2$, *J. Geophys. Res., 87*, 4427, 1982.

Carpenter, D. L., and R. L. Smith, Whistler measurements of electron density in the magnetosphere, *Rev. Geophys., 2*, 415, 1964.

Chang, H. C., and U. S. Inan, A theoretical model study of observed correlations between whistler mode waves and energetic electron precipitation events in the magneosphere, *J. Geophys. Res., 88*, 10,053, 1983.

Chang, H. C., and U. S. Inan, Lightning-induced energetic electron precipitation from the magnetosphere, *J. Geophys. Res., 90*, 1531, 1985a.

Chang, H. C., and U. S. Inan, Test particle modeling of wave-induced energetic electron precipitation, *J. Geophys. Res., 90*, 6409, 1985b.

Chang, H. C., U. S. Inan, and T. F. Bell, Energetic electron precipitation due to gyroresonant interactions in the magnetosphere involving coherent VLF waves with slowly varying frequency, *J. Geophys. Res., 88*, 7037, 1983.

Cornwall, J. M., Scattering of energetic trapped electrons by very low frequency waves, *J. Geophys. Res., 69*, 125, 1964.

Crary, J. H., The effect of the earth-ionosphere waveguide on whistlers, *Tech. Rep. 9*, Stanford Electron. Labs., Stanford Univ., Stanford, Calif., 1961.

Dungey, J. W., Loss of Van Allen electrons due to whistlers, *Planet. Space Sci., 11*, 591, 1963.

Edgar, B. C., The upper and lower frequency cutoffs of magnetospherically reflected whistlers, *J. Geophys. Res., 81*, 205, 1976.

Goldberg, R. J., S. A. Curtis, and J. R. Barcus, Detailed spectral structure of magnetospheric electron bursts precipitated by lightning, *J. Geophys. Res., 92*, 2505, 1987.

Helliwell, R. A., *Whistlers and Related Ionospheric Phenomena*, Stanford University Press, Stanford, Calif., 1965.

Helliwell, R. A., Intensity of discrete VLF emissions, in *Particles and Fields in the Magnetosphere*, edited by B. M. McCormac, p. 292, Reidel, Dordreicht, Holland, 1970.

Helliwell, R. A., J. P. Katsufrakis, and M. L. Trimpi, Whistler-induced amplitude perturbation in VLF propagation, *J. Geophys. Res., 78*, 4679, 1973.

Imhof, W. L., H. D. Voss, M. Walt, E. E. Gaines, J. Mobilia, D. W. Datlowe, and J. B. Reagan, Slot region electron precipitation by lightning, VLF chorus, and plasmaspheric hiss, *J. Geophys. Res., 91*, 883, 1986.

Inan, U. S., Gyroresonant pitch angle scattering by coherent and incoherent whistler mode waves in the magnetosphere, *J. Geophys. Res., 92*, 127, 1987.

Inan, U.S., and D. L. Carpenter, On the correlation of whistlers and associated subionospheric VLF/LF perturbations, *J. Geophys. Res., 91*, 3106, 1986.

Inan, U. S., and D. L. Carpenter, Lightning-induced electron precipitation events observed at $L \simeq 2.4$ as phase and amplitude perturbations on subionospheric VLF signals, *J. Geophys. Res., 92*, 3293, 1987.

Inan, U.S., T.F. Bell, and R.A. Helliwell, Nonlinear pitch angle scattering of energetic electrons by coherent VLF waves in the magnetosphere, *J. Geophys. Res., 83*, 3235, 1978.

Inan, U. S., T. F. Bell, and H. C. Chang, Particle precipitation induced by short-duration VLF waves in the magnetosphere, *J. Geophys. Res., 87*, 6243, 1982.

Inan, U. S., D. L. Carpenter, R. A. Helliwell, and J. P. Katsufrakis, Subionospheric VLF/LF phase perturbations produced by lightning-whistler induced particle precipitation, *J. Geophys. Res., 90*, 7457, 1985a.

Inan, U. S., H. C. Chang, R. A. Helliwell, W. L. Imhof, J. R. Reagan, and M. Walt, Precipitation of radiation belt electrons by man-made waves: A comparison between theory and measurement, *J. Geophys. Res., 90*,359, 1985b.

Leyser, T., U. S. Inan, D. L. Carpenter, and M. L. Trimpi, Diurnal variation of burst precipitation effects on subionospheric VLF/LF signal propagation near $L = 2$, *J. Geophys. Res., 89*, 9139, 1984.

Roberts, C. S., Cyclotron resonance and bounce resonance scattering of electrons trapped in the earth's magnetic field, *Earth's Particles and Fields*, ed. by B. M. McCormac, Reinholdt, New York, 317–336, 1968.

Rycroft, M. J., Enhanced energetic electron intensities at 100 km altitude and a whistler propagating through the plasmasphere, *J. Planet. Space Sci., 21*, 239, 1973.

Tsuruda, K., S. Machida, T. Terasawa, A. Nishida, and K. Maezawa, High spatial attenuation of the Siple transmitter signal and natural VLF chorus observed at ground-based chain stations near Roberval, Quebec, *J. Geophys. Res., 87*, 742, 1982.

Voss, H. D., J. B. Reagan, W. L. Imhof, D. O. Murray, D. A. Simpson, D. P. Cauffman, and J. C. Bakke, Low temperature characteristics of solid state detectors for energetic x-ray, ion and electron spectrometers, *IEEE Trans. Nucl. Sci., NS-29*, 164, 1982a.

Voss, H. D., J. C. Bakke, and S. N. Roselle, A spacecraft multichannel analyzer for a multidetector solid state detector array, *IEEE Trans. Nucl. Sci. NS-29*, 173, 1982b.

Voss, H. D., W. L. Imhof, J. Mobilia, E. E. Gaines, M. Walt, U. S. Inan, R. A. Helliwell, D. L. Carpenter, J. P. Katsufrakis, and H. C. Chang, Lighting-induced electron precipitation, *Nature, 312*, 740, 1984.

W. L. Imhof, H. D. Voss, and M. Walt, Lockheed Palo Alto Research Laboratory, Palo Alto, CA 94304.

U. S. Inan, Space, Telecommunications, and Radioscience Laboratory, Department of Electrical Engineering/SEL, Stanford University, Durand 324, Stanford, CA 94305.